A Computational Study of the Spreading of Oil Underneath a Sheet of Ice

Mark Sussman
Department of Mathematics
University of California Davis
Davis, CA 95616

Shotaro Uto
Arctic Vessel and Low Temperature Engineering Division
Ship Research Institute
6-38-1, Shinkawa, Mitaka
Tokyo 181, Japan
(November 16, 1998)

The spreading of oil underneath a sheet of ice is computed using an adaptive level set method for incompressible two-fluid flow. Factors such as viscosity, surface tension, and wall adhesion are taken into account in the computations. The results of the computations agree well with previous experiments and theory. In this work, we also present a very efficient and accurate computational method for determining the final steady profile of a body of oil under ice in water. The computational models are used to make further observations regarding the dependency of the oil spreading radius on the surface energies between the oil, ice, and water.

I. INTRODUCTION

In recent years there has been increased oil excavation in ice covered waters [20,9]. As a result, chances are increased that an oil spill due to a tanker accident or the rupture of an oil pipeline will occur in ice covered waters. It is generally known that oil spreads over a much smaller area under the ice cover than in open waters [9]. Although the presence of an ice cover results in reduced spreading of oil, the presence of an ice cover also makes it difficult in determining the location and area of the oil slick. Estimating the extent of the oil slick is indispensable to the recovery of oil spreading under the ice cover [9].

The important factors determining the spreading rate of oil under ice are the viscosity of oil, the volume of oil, and the relative surface energies between the oil, water and ice. In experiments by Yapa and Chowdhury [20] and Izumiyama et al. [9], oil is poured through a hole in a layer of ice, and then the oil's spreading radius underneath the ice is measured. In Figure 1 we sketch a diagram of axi-symmetrical spreading of oil underneath a solid ice cover. The parameters varied in their experiments [20,9] were oil viscosity, pouring rate of oil, and volume of oil. Unfortunately, it is difficult to quantify the effect of surface tension and wall adhesion from their experiments, because the oil-water interfacial tension and the contact angle that the free-surface forms with an ice surface were not reported by Yapa and Chowdhury or Izumiyama et al. In experiments by Liukkonen [11] and Kniazeva [10], oil droplets were placed under an inclined ice cover in order to determine the oil-water interfacial tension and contact angle. They observed representative values of 49.2g/s^2 for the oil-water interfacial tension and 160^o for the contact angle. These values may not represent the values used in experiments [20,9]. According to Uzuner et al. [19], the oil-water interfacial tension γ may take on values ranging from 15.8g/s^2 to 69g/s^2. Furthermore, there is speculation [11] that there is really a thin layer of water between the oil and ice; this implies that the contact angle might be 180^0 and not 160^o.

Along with experiments, theoretical models have been developed by Kniazeva [10], Yapa and Chowdhury [20] and Izumiyama et al. [9]. In their work, equations were developed which describe the oil spreading radius in terms of the viscosity of the oil, net interfacial tension, rate of discharge of the oil, and the volume of oil present in the slick.

In our work, we study the spreading of oil under ice by computational methods. Currently we know of only one reference, Kniazeva [10], of computational work done on oil spreading under ice. Many simplifications were made in Kniazeva's computational model. For example, in Kniazeva's model, the thickness of the oil slick was assumed to be constant throughout the extent of the slick. In this work, we use two computational methods for studying the spreading of oil under ice in water. The first method, an adaptive level set approach [13], solves the full Incompressible Navier-Stokes equations for two-fluid flow. The adaptive level set approach allows us to easily vary important parameters such as the inflow rate of oil, volume of oil present in the slick, viscosity, oil-water interfacial tension, and contact angle. The second method, a new energy minimization approach, solves for the final *static* profile of the oil/water free surface. The second method takes into account the density jump across the oil/water interface and also takes into account the relative surface energies of the oil, water and ice. Since our second method is specialized for the static oil droplet problem, it is much more efficient, and accurate then the adaptive level set approach for computing the final shape of a body of oil under ice.

II. THEORETICAL APPROACH

In this section, we give an overview of the theory developed by Yapa and Chowdhury [20] and Izumiyama et al. [9], for predicting the extent of oil spreading under ice covered waters. In their work the Navier-Stokes equations for steady, axisymmetric, incompressible flow are used to model the oil,

$$uu_r + vu_z = -\frac{1}{\rho_o}p_r + \nu_o(u_{rr} + \frac{u_r}{r} - \frac{u}{r^2} + u_{zz}) \quad (1)$$

$$uv_r + vv_z = -\frac{1}{\rho_o}p_z + \nu_o(v_{rr} + \frac{v_r}{r} + v_{zz}) + g \quad (2)$$

$$\frac{(ru)_r}{r} + v_z = 0. \quad (3)$$

Here, u is the radial velocity, v is the vertical velocity, ρ_o is the density of oil, and $\nu_o = \mu_o/\rho_o$ is the kinematic viscosity for oil. Since the oil slick radius $R(t)$ is much larger than the slick thickness h, we introduce two dimensional length scales $z^* << r^*$ into (1) thru (3). As a result of eliminating low order terms from (1) thru (3), the following simplified equations follow,

$$\frac{1}{\rho_o}p_r = \nu_o u_{zz} \quad (4)$$

$$\frac{1}{\rho_o}p_z = g \quad (5)$$

$$\frac{(ru)_r}{r} = 0, \quad (6)$$

along with the no slip boundary condition at the ice,

$$u(r, 0) = 0, \quad (7)$$

and the following assumption for the tangential velocity at the oil-water interface,

$$u(r, -h) = u_i(r). \quad (8)$$

The resulting solution of the simplified equations is

$$u(r,z) = -\frac{u_i z}{h}(1+\lambda(1+\frac{z}{h})) \tag{9}$$

where λ is a constant defined to be

$$\lambda = -\frac{\partial p}{\partial r}\frac{h^2}{2\mu_o u_i}. \tag{10}$$

We define $\bar{u}_i$ as the average interfacial velocity between the oil and water,

$$\bar{u}_i = \frac{1}{\pi R^2(t)}\int_0^{R(t)} 2\pi r u_i dr. \tag{11}$$

The shear stress $\partial u/\partial z$ at $z=0$ and $z=-h$ is used to find the total viscous force retarding the spread of oil

$$F_v = -\frac{\mu_o \bar{u}_i \pi R^2}{h}. \tag{12}$$

The buoyancy force accelerating the spread of oil is

$$F_g = \frac{1}{2}\pi R h^2 g(\rho_w - \rho_o). \tag{13}$$

During the gravity-viscous phase $F_v + F_g = 0$; therefore

$$\bar{u}_i = \frac{(\rho_w - \rho_o)gh^3}{2\mu_o R}. \tag{14}$$

If we assume that

$$\bar{u}_i \propto \frac{dR(t)}{dt}, \tag{15}$$

and the discharge rate of oil,

$$Q = \frac{\pi R^2 h}{t}, \tag{16}$$

is constant, then

$$R(t) = k\left[\frac{(\rho_w - \rho_o)gQ^3}{\mu_o}\right]^{1/8} t^{1/2}. \tag{17}$$

Equation (17) represents the solution for "constant discharge mode" when Q is constant. In "constant volume mode," $Q=0$, the final slick radius R_f can be determined by balancing the buoyancy force F_g with the force due to the net interfacial tension F_t. According to Yapa and Chowdhury,

$$V = \pi R^2 h \tag{18}$$

$$F_t = \pi R_f \sigma_n \tag{19}$$

$$R_f = (\frac{1}{2\pi^2})^{1/4}\left[\frac{(\rho_w - \rho_o)g}{\sigma_n}\right]^{1/4} V^{1/2}. \tag{20}$$

Here σ_n represents the "net interfacial tension" which is derived from oil-water (γ), ice-water, and ice-oil interfacial tensions. The "net interfacial tension" is also derived from the surface roughness of the ice ϵ.

In recent work by Izumiyama et al. [9] extensions were made to the model prescribed by Yapa and Chowdhury (17) in order to include the effects of the net interfacial tension. They observed in their experiments that the slope of the graph of R versus $\sqrt{t}$ did not behave as predicted by (17). In our computations, we observed the same phenomena when we measured the spreading constant k, defined in (17), for different numerical simulations when the surface tension coefficient γ or the contact angle θ was varied; see Table VI. It is evident that when γ or θ are increased, k decreases.

In the modified approach of Izumiyama et al., the force due to the net interfacial tension (19) is also included along with the total viscous force (12) and the buoyancy force (13):

$$F_v + F_g = F_t. \tag{21}$$

The modified equation for the spreading rate in "constant discharge mode," is

$$R(t) = k_1\left[\frac{(\rho_w - \rho_o)gQ^3}{\mu_o}\right]^{1/8} f(\alpha)t^{1/2}, \tag{22}$$

where

$$f(\alpha) = \left(\alpha + 1 - (\alpha^2 + 2\alpha)^{1/2}\right)^{1/8} \tag{23}$$

and

$$\alpha = \pi\frac{\sigma_n^2}{(\rho_w - \rho_o)g\mu_o Q}. \tag{24}$$

III. GOVERNING EQUATIONS FOR NUMERICAL METHODS

We assume that both the water and oil are governed by the incompressible Navier-Stokes equations; therefore,

$$\begin{aligned}\rho_w\frac{D\boldsymbol{U}_w}{Dt} &= -\nabla p_w + 2\mu_w\nabla\cdot\mathcal{D} + \rho_w\boldsymbol{F}\\ \nabla\cdot\boldsymbol{U}_w &= 0\end{aligned} \tag{25}$$

for all points in the liquid and,

$$\begin{aligned}\rho_o\frac{D\boldsymbol{U}_o}{Dt} &= -\nabla p_o + 2\mu_o\nabla\cdot\mathcal{D} + \rho_o\boldsymbol{F}\\ \nabla\cdot\boldsymbol{U}_o &= 0\end{aligned} \tag{26}$$

for all points in the oil.

$\boldsymbol{U}$ is the velocity, p is the pressure, ρ is the density, and μ is the viscosity of the fluid. The subscripts w and o denote water and oil, respectively. D/Dt is the material derivative, $\mathcal{D}$ is the rate of deformation tensor, and $\boldsymbol{F}$ is the acceleration due to gravity. The boundary conditions at the interface, Γ, between oil and water are

$$(2\mu_w\mathcal{D} - 2\mu_o\mathcal{D})\cdot\boldsymbol{n} = (p_w - p_o + \gamma\kappa)\boldsymbol{n}$$
$$\boldsymbol{U}_w = \boldsymbol{U}_o, \tag{27}$$

where $\boldsymbol{n}$ is the unit normal to the interface drawn from the oil to the water, $\kappa = \nabla\cdot\boldsymbol{n}$ is the curvature of the interface, and γ is the coefficient of surface tension between oil and water.

We will denote the domain containing the two fluids as Ω and its boundary as $\partial\Omega$. At solid wall boundaries, the no-slip boundary condition holds,

$$\boldsymbol{U} = 0 \qquad \text{on} \qquad \partial\Omega. \tag{28}$$

Besides the no-slip boundary condition, we must specify a contact angle (θ) at the point where the oil-water interface meets the solid boundary. The contact angle is a constant derived by previous experiments [11]. Figure 2 displays an example configuration.

IV. ENERGY MINIMIZATION APPROACH FOR COMPUTING STATIC OIL DROPLETS

In this section, we describe the "energy minimization approach", which is a new efficient method for computing the final profile of a body of oil under ice, surrounded by water. We will assume axisymmetric geometry. Since we are concerned with the static solution in this section, the time derivative terms, advection terms and viscous terms in (25) and (26) are dropped. The resulting problem reduces to the minimization of the following energy,

$$E(r(z),h) = \int_0^h (\rho_w - \rho_o)g\pi z r^2 + 2\pi r\gamma\sqrt{1+[r'(z)]^2}dz + \gamma\pi(\sin(\theta-\pi/2)r^2(0) + r^2(h)), \tag{29}$$

subject to the constraint,

$$\int_0^h \pi r^2 dz = V. \tag{30}$$

Here, $z = 0$ represents the coordinant of the ice surface and $z = h$ represents the bottom of the oil layer. In other words, h is the thickness of the oil slick.

As a remark, θ and γ may be given in terms of the relative surface energies of the oil, water and ice. If γ_{iw}, γ_{io}, and γ_{ow} are the surface energies between the ice/water, ice/oil, and oil/water interfaces respectively, then using the Young-Dubre equation, we have,

$$\gamma \equiv \gamma_{ow} \tag{31}$$
$$\sin(\theta-\pi/2)\gamma \equiv (\gamma_{io} - \gamma_{iw}). \tag{32}$$

We discretize (29), by minimizing the discretized energy equation,

$$E(\vec{r},h) = \sum_{i=0}^{N-1}(\rho_w-\rho_o)g\pi r_{i+1/2}^2 z_{i+1/2}\Delta z + \sum_{i=0}^{N-1} 2\pi\gamma r_{i+1/2}\sqrt{1+[\frac{r_{i+1}-r_i}{\Delta z}]^2}\Delta z + \gamma\pi(\sin(\theta-\pi/2)r_0^2 + r_N^2), \tag{33}$$

subject to the constraint,

$$\sum_{i=0}^{N-1}\pi r_{i+1/2}^2\Delta z = V. \tag{34}$$

Here, $\vec{r}$ represents the unknown quantities, $r_0, r_1, \ldots, r_N$ where $r_i = r(ih/N)$. $r_{i+1/2}$ and Δz are defined as $(r_i + r_{i+1})/2$ and h/N respectively.

In order to solve the minimization problem, we use (34) in order to express the oil slick thickness h in terms of the unknowns $\vec{r}$,

$$h(\vec{r}) = \frac{VN}{\sum_{i=0}^{N-1}\pi r_{i+1/2}^2}. \tag{35}$$

We then plug our expression for h (35) back into (33) so that we can express energy only in terms of the unknowns $\vec{r}$. In order to minimize (33), we solve,

$$\frac{\partial E(\vec{r},h(\vec{r}))}{\partial r_i} = 0 \qquad i = 0\ldots N. \tag{36}$$

We solve (36) by using the Newton Iteration method:

$$\vec{r}^{n+1} = \vec{r}^n - J^{-1}\vec{f}(\vec{r}). \tag{37}$$

J is the Jacobian matrix whose components are,

$$J_{ij} = \frac{\partial^2 E(\vec{r},h(\vec{r}))}{\partial r_i \partial r_j}. \tag{38}$$

$\vec{f}(\vec{r})$ is a vector defined as,

$$f_i(\vec{r}) \equiv \frac{\partial E(\vec{r},h(\vec{r}))}{\partial r_i}. \tag{39}$$

One should not be careless in choosing the initial iterate $\vec{r}^0$ for the Newton Iteration. We initialize $\vec{r}^0$ to be constant for all z; in other words,

$$r_i^0 = R_0 \qquad i = 0\ldots N. \tag{40}$$

R_0 is determined by minimizing (29) over the class of functions $r(z)$ which are *constant*. The resulting equation for R_0 is

$$R_0^4 - \frac{V}{\pi(1+\sin(\theta-\pi/2))}R_0 - \frac{(\rho_w-\rho_o)gV^2}{2\pi^2\gamma(1+\sin(\theta-\pi/2))} = 0. \tag{41}$$

As a remark, for $V >> 1$, (41) reduces to (20) where

$$\sigma_n = \gamma(1 + \sin(\theta - \pi/2)). \tag{42}$$

The advantages of the "energy minimization approach" is that it is very fast and very accurate. We have needed at most 20 Newton Iterations in order to reach the convergence tolerance of 10^{-8}. This includes computations of steady profiles where θ ranges from 0.1^0 up to 180^0. Since we only discretize for $0 \le z \le h$, we can accurately compute the final spreading radius, and profile, for oil slicks where the final spreading radius is much bigger than the thickness h. We can also accurately compute the final spreading radius and profile, for oil slicks on top of ice as well as below ice where the contact angle θ is typically 10^0. In this case, as with the case for large oil spills under ice, the final spreading radius R_f will be much larger than the thickness h.

A disadvantage of the "energy minimization approach" is that it is not applicable to general topologies of the free surface. For example, in the work of Zhao et al. [21], a level set method was presented for finding the final shape of multiple bubbles in a more general geometry. Another disadvantage of our "energy minimization approach" is that it is only applicable for the static problem. Below we describe the "Adaptive Level Set approach" for solving the unsteady problem of oil spreading under ice.

V. ADAPTIVE LEVEL SET APPROACH

A. Level Set Formulation

We use the level set function [12,16], for tracking the interface between oil and water. In our algorithm the interface Γ, is the zero level set of ϕ:

$$\Gamma = \boldsymbol{x} | \phi(\boldsymbol{x}, t) = 0.$$

The level set function ϕ is positive in the water and negative in the oil. Hence we have

$$\phi(\boldsymbol{x}, t) \quad \begin{cases} > 0 & \text{if } \boldsymbol{x} \in \text{the water} \\ = 0 & \text{if } \boldsymbol{x} \in \Gamma \\ < 0 & \text{if } \boldsymbol{x} \in \text{the oil.} \end{cases} \tag{43}$$

The unit normal on the interface, drawn from the oil into the water, and the curvature of the interface can easily be expressed in terms of $\phi(\boldsymbol{x}, t)$

$$\boldsymbol{n} = \left. \frac{\nabla \phi}{|\nabla \phi|} \right|_{\phi=0} \quad \text{and} \quad \kappa = \nabla \cdot \left(\left. \frac{\nabla \phi}{|\nabla \phi|} \right) \right|_{\phi=0}.$$

Next, we let

$$\boldsymbol{u} = \begin{cases} \boldsymbol{u}_\ell & \phi > 0 \\ \boldsymbol{u}_g & \phi \le 0, \end{cases}$$

where $\boldsymbol{u}$ is called the fluid velocity. By virtue of the boundary conditions, $\boldsymbol{u}$ is continuous across the interface. Since the interface moves with the fluid particles, the evolution of ϕ is then given by

$$\frac{\partial \phi}{\partial t} + \boldsymbol{u} \cdot \nabla \phi = 0. \tag{44}$$

The governing equation for the fluid velocity, $\boldsymbol{u}$, along with the boundary conditions can be written as a single equation:

$$\rho(\phi) \frac{D\boldsymbol{u}}{Dt} = -\nabla p + \nabla \cdot (2\mu(\phi)\mathcal{D}) - \gamma \kappa(\phi) \delta(\phi) \nabla \phi + \rho(\phi) \boldsymbol{F}, \tag{45}$$

where ρ and μ are, respectively, the density and viscosity and δ is the Dirac delta function. The surface tension force is interpreted as a body force localized on the interface. By $\kappa(\phi)$ we mean

$$\kappa(\phi) = \nabla \cdot \left(\frac{\nabla \phi}{|\nabla \phi|} \right).$$

Since the density and viscosity are constant in each fluid, they take on two different values depending on the sign of ϕ; hence we write

$$\rho(\phi) = \rho_o + (\rho_w - \rho_o) H(\phi) \tag{46}$$

and

$$\mu(\phi) = \mu_o + (\mu_w - \mu_o) H(\phi), \tag{47}$$

where $H(\phi)$ is the Heaviside function given by

$$H(\phi) = \begin{cases} 0 & \text{if } \phi < 0 \\ \frac{1}{2} & \text{if } \phi = 0 \\ 1 & \text{if } \phi > 0. \end{cases} \tag{48}$$

The Navier-Stokes equations for two-fluid flows was written in similar form and used by Unverdi & Tryggvason (1992) [18]. The fact that the surface tension can be written as a delta function concentrated at the interface has been used by Unverdi & Tryggvason (1992) and Brackbill, Kothe, & Zemach (1992) [7]. The form we use here is due to Chang, Hou, Merriman, & Osher [8]. The derivation of equation (45) can be found in Chang *et al.* in which it is shown that the formulation of (45) admits solutions which are consistent with the free-surface boundary conditions (27).

B. Discretization

In order to discretize (45), we use the variable density projection method as described by Bell et al. [4], Bell and Marcus [5] and Almgren et al. [2].

The discrete velocity field $\boldsymbol{U}^n_{i,j}$ and the discrete level set function $\phi^n_{i,j}$ are located at cell centers. The pressure $p^{n-1/2}_{i+1/2,j+1/2}$ is located at cell corners. A diagram of

where the discrete variables are located in relation to the computational grid is shown in Figure 3. J represents the index of the computational cell closest to the top wall.

The time stepping procedure is based on the Crank-Nicholson method. Since the viscosity in oil is much larger than that in water, we modify the Crank-Nicholson procedure by handling the viscous terms implicitly as opposed to semi-implicitly. By computing the viscous terms implicitly, we avoid large restrictions on the time step. Given $\boldsymbol{U}^n$, ϕ^n and $p^{n-1/2}$ at time $t = t^n$, we discretize (45) and (44) in time using the following steps:

1. Update the location of the interface by solving

$$\phi^{n+1} = \phi^n - \Delta t[\boldsymbol{U} \cdot \nabla\phi]^{n+\frac{1}{2}}. \tag{49}$$

The nonlinear advection term

$$[\boldsymbol{U} \cdot \nabla\phi]^{n+\frac{1}{2}}, \tag{50}$$

is approximated using a second order upwind scheme described by Bell and Marcus [5]. In order to predict the nonlinear term (50) at the half time level, a Taylor series expansion of the state variables is used. For example,

$$\phi^{n+1/2} \approx \phi^n + \frac{\Delta t}{2}\phi_t^n = \phi^n + \frac{\Delta t}{2}(-\boldsymbol{U} \cdot \nabla\phi)^n. \tag{51}$$

2. Viscous solve:

$$\frac{\boldsymbol{U}^* - \boldsymbol{U}^n}{\Delta t} = -[(\boldsymbol{U} \cdot \nabla)\boldsymbol{U}]^{n+\frac{1}{2}} - \frac{\nabla p^{n-\frac{1}{2}}}{\rho^{n+\frac{1}{2}}} + \frac{\nabla \cdot (2\mu^{n+\frac{1}{2}}\mathcal{D}^*)}{\rho^{n+\frac{1}{2}}} - \frac{\kappa(\phi^{n+\frac{1}{2}})\nabla H^{n+\frac{1}{2}}}{\rho^{n+\frac{1}{2}}} + \boldsymbol{F}. \tag{52}$$

As with the discretization of (49), the nonlinear advection term

$$[(\boldsymbol{U} \cdot \nabla)\boldsymbol{U}]^{n+\frac{1}{2}} \tag{53}$$

is approximated using a second order upwind scheme. Equation (52) when discretized results in a matrix system that is solved for both components of $\boldsymbol{U}^*$. We use Multigrid as an iteration method for solving (52).

3. Projection step:
The following equation is solved for p,

$$\nabla \cdot \frac{\nabla p}{\rho^{n+\frac{1}{2}}} = \nabla \cdot \frac{\boldsymbol{U}^* - \boldsymbol{U}^n}{\Delta t}. \tag{54}$$

The new velocity and pressure at time t^{n+1} are updated as:

$$\frac{\boldsymbol{U}^{n+1} - \boldsymbol{U}^n}{\Delta t} = \frac{\boldsymbol{U}^* - \boldsymbol{U}^n}{\Delta t} - \frac{\nabla p}{\rho^{n+\frac{1}{2}}} \tag{55}$$

$$p^{n+1/2} = p^{n-1/2} + p. \tag{56}$$

The matrix system of equations that result from discretizing (54) are solved using the Multigrid Preconditioned Conjugate Gradient Method [17].

4. Reinitialize the level set function.
While the level set function ϕ is initialized as the signed distance to the free surface, under the evolution of (44) it will not remain so. We solve the following equation [16]

$$\phi_\tau = \text{sign}(\phi)(1 - |\nabla\phi|), \tag{57}$$

where τ is an artificial time $\tau = 0 \ldots \epsilon$, in order to maintain the level set function as a distance function for points within ϵ of the free surface. A justification for maintaining the level set function as a distance function is given in section V B 1, "thickness of the interface."

1. Thickness of the Interface

In order to solve (45) numerically we must modify it slightly due to the sharp changes in ρ across the front and also because of the numerical difficulties presented by the Dirac delta function contained in (45). To alleviate these problems we shall give the interface a fixed thickness that is proportional to the spatial mesh size. This allows us to replace $\rho(\phi)$ by a smoothed density, $\rho_\epsilon(\phi)$, which is given by

$$\rho_\epsilon(\phi) = \rho_o + (\rho_w - \rho_o)H_\epsilon(\phi), \tag{58}$$

with

$$H_\epsilon(\phi) = \begin{cases} 0 & \text{if } \phi < -\epsilon \\ \frac{1}{2}[1 + \frac{\phi}{\epsilon} + \frac{1}{\pi}\sin(\pi\phi/\epsilon)] & \text{if } |\phi| \le \epsilon \\ 1 & \text{if } \phi > \epsilon. \end{cases} \tag{59}$$

The smoothed or mollified delta function is

$$\delta_\epsilon(\phi) = \frac{dH_\epsilon}{d\phi}. \tag{60}$$

It is clear from (59) that the thickness of the interface is approximately

$$\frac{2\epsilon}{|\nabla\phi|}. \tag{61}$$

In our algorithm the front will have a uniform thickness, consequently we must have $|\nabla\phi| = 1$ when $|\phi| \le \epsilon$. A function that satisfies

$$|\nabla d| = 1 \quad \text{for} \quad \boldsymbol{x} \in \Omega \quad \text{with} \quad d = 0 \quad \text{for} \quad \boldsymbol{x} \in \Gamma \tag{62}$$

is called a distance function. This is because d is the signed normal distance to the interface, Γ.

If a level set function is equal to a distance function it then follows from (59) that the thickness of the interface is 2ϵ. In our numerical calculations we shall take $\epsilon = \alpha\Delta x$ where Δx is the grid size. Therefore, the interface will reduce in thickness as we refine our mesh.

Therefore it seems ideal to choose the level set function to be a distance function. It is clear that we can choose $\phi(\boldsymbol{x}, 0)$ to be a distance function; however, under the evolution of (44) it will not necessarily remain as such. We must then be able to solve the following problem: given a level set function, $\phi(\boldsymbol{x})$, reinitialize it to be a distance function *without changing its zero level set*. This can be achieved by solving the following partial differential equation:

$$\frac{\partial d}{\partial \tau} = \text{sign}(\phi)(1 - |\nabla d|), \tag{63}$$

with initial conditions

$$d(\boldsymbol{x}, 0) = \phi(\boldsymbol{x}),$$

where

$$\text{sign}(\phi) = \begin{cases} -1 & \text{if } \phi < 0 \\ 0 & \text{if } \phi = 0 \\ 1 & \text{if } \phi > 0 \end{cases} \tag{64}$$

and τ is an artificial time. It is clear from (59) that we need only ϕ to be a distance function close to the front. The solution $d(\boldsymbol{x}, \epsilon)$ will be a distance function for $|d| \leq \epsilon$. Furthermore, since $\text{sign}(0) = 0$, $d(\boldsymbol{x}, \epsilon)$ has the same zero level set as $\phi(\boldsymbol{x})$. Therefore we simply solve (63) for $\tau = 0 \ldots \epsilon$, and then replace $\phi(\boldsymbol{x})$ by $d(\boldsymbol{x}, \epsilon)$.

2. Contact Angle Boundary Conditions

Consider figure 4. For contact angles $\theta = 90^0$, the level set function can be well defined as a distance function for any point in the oil or water. This is because at any point (x, y) in the computational domain, a normal can be drawn from the oil/water interface to the point (x, y). If $\theta < 90^0$, then the level set function cannot be well defined as a distance function at points (x, y) that lie on the water/ice boundary. If $\theta > 90^0$, then the level set function cannot be well defined as a distance function at points (x, y) that lie on the oil/ice boundary. For the cases when $\theta \neq 90^0$, we construct an imaginary interface which is denoted as the dashed line in figure 4. The points "P" and "Q" are found via second order extrapolation of the level set function.

In order to implement the imaginary interface in figure 4, we use appropriate boundary conditions for d when solving the redistance equation (63) and for ϕ when discretizing the curvature and advection terms. We initialize the "ghost cells" $d_{i,j}$ $(j > J)$ by setting $d_{i,j}$ equal to the signed distance to the imaginary interface. For ghost cells (i, j) in which a normal cannot be drawn from the imaginary interface to (x_i, y_j), we initialize $d_{i,j}$ to be the second order extrapolation of d from the interior of the computational domain.

3. Mass Conservation

In preliminary computations of oil spreading using our numerical method, we experienced a maximum of 5% overall mass loss using our numerical method. This error is prevalent due to the high contact angle we must enforce; $\theta = 160^0$ or $\theta = 175^o$. The high contact angle induces large gradients in the level set function at the point where the free surface meets the ice. A 5% mass loss translates into about a 7% error in the final spreading radius R_f for our computations; this error is unacceptable for our study. In order to conserve mass exactly, we did the following steps after each time step:

1. Find the zero contour of the level set function ϕ using bilinear interpolation. The zero contour will consist of piecewise linear line segments.

2. Determine the oil mass $M(t)$ and perimeter $P(t)$ from the piecewise linear contour constructed from step 1.

3. Determine the expected mass $M_{exact}(t)$ of oil. For our simulations, $M_{exact} = M(0) + \pi r_{orifice}^2 v_{inflow} t$. $r_{orifice}$ is the radius of the "hole" into which oil is added. v_{inflow} is the normal velocity of oil entering the "hole."

4. Update the level set function:

$$\phi = \phi + \frac{1}{2}\frac{M(t) - M_{exact}(t)}{P(t)} \tag{65}$$

Our algorithm for enforcing mass conservation did not have any adverse effects in the spreading rate $R(t)$. As shown in sections VI B and VI C, our results agree well with experiments and theory. The maximum mass fluctuation after imposing our fix for mass conservation is 2 parts in ten thousand.

C. Adaptive Mesh Refinement

In the problems we wish to solve, the thickness of the oil layer can be very thin in relation to its length. Furthermore, for simulations where the discharge rate Q is constant, only a small portion of the physical domain will be covered with oil during early times. In order to efficiently simulate oil spreading, we use adaptive mesh refinement [1,13] to add resolution to regions near the oil/water interface.

In figure 5 we show an example of the grid structure used in adaptive mesh refinement. The grid hierarchy is composed of different levels of refinement ranging from coarsest ($\ell = 0$) to finest ($\ell = \ell_{max}$). The coarsest level ($\ell = 0$) covers the whole computational domain while successively higher levels ($\ell + 1$) lie on top of the level underneath them (level ℓ). Each level is represented as the union of rectangular grid patches of a given resolution. In our computations the refinement ratio between levels is 2. Thus we have $\Delta x^{\ell+1} = \Delta y^{\ell+1} = \frac{1}{2}\Delta x^{\ell}$.

The initial creation of the grid hierarchy and the subsequent regridding operations in which the grids are dynamically changed to reflect changing flow conditions use the same procedures as were used by Bell et al. [3] for hyperbolic conservation laws. In the problems we compute here, we shall "tag" cells which contain part of the oil/water interface, i.e. those in which the level set function changes sign. Once cells on a specified level are "tagged" for refinement, the grids at the next higher level can be constructed. The tagged cells are grouped into rectangular patches using the clustering algorithm given in Berger and Rigoustsos [6]. These rectangular patches are refined to form the grids at the next level. The process is repeated until either the error tolerance criteria are satisfied or a specified maximum level is reached.

At $t = 0$ the initial data is used to create grids at level 0 through ℓ_{max}. As the solution advances in time, the regridding algorithm is called every step to redefine grids at levels 1 to ℓ_{max}. Level 0 grids remain unchanged throughout the calculation.

When new grids are created at level $\ell + 1$, the data on these new grids are copied from the previous grids at level $\ell + 1$ if possible, otherwise interpolated in space from the underlying level ℓ grids.

The procedure to advance $\boldsymbol{U}$ and ϕ on levels 0 thru ℓ_{max} is similar to that presented for the single grid discretization described in section V B. The evaluation of the advective derivatives found in in (53) and (50) can be performed one grid at a time, with boundary data copied from other fine grids, interpolated from underlying coarse grids, or supplied from physical boundary conditions. Since the redistance operation (57) is discretized as an advection equation, the same procedure as for handling the advective terms may be applied to handling the level set reinitialization too. The parabolic (52) and single-level elliptic solve (54) require that the solution be computed on all grids at a level at one time, since these are no longer explicit operations. Boundary data for these solves are interpolated from underlying coarse grids or supplied from physical boundary conditions.

VI. RESULTS

A. Validation

The level set method has been validated against a variety of air-water flows for axisymmetric and fully 3d flows [16,15,14,13]. Examples of problems tested with the level set method include surface tension driven drop dynamics, water drop impacting on a pool of water, and the flow of a gas bubble rising to a water surface and then "bursting." In this section, we focus on validation of our approach for handling the contact angle boundary condition which is a new feature of our level set method.

We shall consider the relaxation of an oil droplet in water placed underneath an ice cover. The user-defined contact angle boundary condition between the free-surface and the ice will be $\theta = 160^o$. The surface tension coefficient γ is $49.2g/s^2$. These are the experimental values observed by Liukkonen [11] for a 0.2cm^3 droplet of fresh crude oil lying underneath an ice cover.

The oil droplet is initialized underneath an ice cover in such a way that it intersects the ice cover at a 90^o angle. The initial shape of the droplet is a semi-sphere. The volume of the oil drop is 0.2cm^3, the viscosity μ_o is $0.315\text{g}/(\text{cm}\cdot\text{s})$, the density ρ_o is $0.85\text{g}/\text{cm}^3$, and gravity g is $980\text{cm}/\text{s}^2$. The parameters for water are $\mu_w = 1.792 \times 10^{-2}\text{g}/(\text{cm}\cdot\text{s})$ and $\rho_w = 1.00\text{g}/\text{cm}^3$. Here, since the initial contact angle is 90^0 and the user-defined contact angle is $\theta = 160^o$, the contact position will begin to decrease. Eventually buoyancy forces arrest the shrinking of the contact position. In figures 6 and 7 we display the profile of the oil droplet at $t = 0.0$ and $t = 1.2$ respectively. In figures 8 and 9 we display the contact position and kinetic energy versus time respectively when using the level set method. As a note, the dark contour in figure 7, represents results using the "Energy Minimization Approach" with $N = 128$. The results using the two methods are almost indistinguishable.

We ran this problem using successively higher levels of resolution. In Table I, we list the final steady contact position of the droplet for resolutions of 32x32, 64x64 and 128x128 when using the level set approach. Besides measuring the final contact position for the relaxation from an initial angle of 90^0, we also measured the final contact position for the relaxation from an initial angle of 160^o. As shown in Table I, these results are almost identical to the first case.

In Table II, we list the final steady contact position for a relaxing oil droplet under similar conditions as in Table I, except that we used the "energy minimization approach" instead of the level set approach. The time to completion in order to find the final steady profile was orders of magnitude smaller using the "energy minimization approach" as compared to the level set approach. What is remarkable about the similarity between the results when using either of our approaches, is the fact that the "energy minimization approach" does not ex-

plicitly enforce the contact angle as does the level set approach; instead, the contact angle is implicitly enforced thru proper specification of the surface energy between the ice and the oil.

B. Spreading simulation; Comparison with experiments

In this section we compute the spreading of oil under an ice cover and compare our computed spreading radius $R(t)$ to the radius obtained from experiments. We use an axisymmetric coordinant system and our computational domain is 32cm by 8cm. We have inflow conditions at the top boundary, which is the ice boundary, for $r \leq r_{orifice}$. $r_{orifice}$ is the radius of the "hole" into which oil is poured into the computational domain. The inflow velocity is specified as $v_{inflow} = Q/(\pi r_{orifice}^2)$. Q is the user specified average inflow rate (cm^3/s).

In Figure 10, we show representative profiles of a computation of oil spreading under ice at different times. The boxes in Figure 10 represent levels of adaptivity; the effective resolution at the finest level of adaptivity is 128x32. The user-specified parameters for this problem are $\theta = 160^0$, $\gamma = 49.2 g/s^2$,$Q = 24.6 cm^3/s$, $\mu_o = 2.54 g/(cm \cdot s)$, $\mu_w = 1.792 \times 10^{-2} g/(cm \cdot s)$, $\rho_o = 0.878 g/cm^3$, and $\rho_w = 1.001 g/cm^3$. These parameters correspond to experiment 6, Table 1 in Izumiyama et al. [9]. In Figure 12, we plot the spreading radius $R(t)$[1] versus $\sqrt{t}$ for the computation shown in Figure 10. As predicted by (17), the graph is a straight line. The spreading constant k (17) is 0.46 as measured from the slope of our graph in Figure 12. This compares well with the experimental [9] result of $k = 0.45$. For measuring the final slick radius R_f, we used the "energy minimization approach" described in section IV. In Figure 11, we display the computed final steady profile of the oil slick; the final slick radius is $R_f = 27.8$ which compares well with the experimental [9] value of $R_f = 26.7$cm. In Table III, we show more comparisons of our computational results with those of experiments [9,20]. We suspect that any discrepancy between our computations and experiments is because our values for the surface tension coefficient $\gamma = 49.2 g/s^2$ and user-specified contact angle $\theta = 160^o$ are not representative of the machine oil used in the experiments [9]. We chose the values for γ and θ based on observations by Liukkonen [11]. According to Uzuner et al. [19], γ may take on values ranging from $15.8 g/s^2$ to $69 g/s^2$. Furthermore, there is speculation that there is really a thin layer of water between the oil and ice; this implies that the user-specified contact angle might be 180^0 and not 160^o.

[1]We measure $R(t)$ from our spreading computations as the *front* of our oil "slick"; not as the point where the free surface meets the ice

C. Spreading simulation; Comparison with theory

In this section we compute the spreading of oil under an ice cover and compare our computed spreading radius $R(t)$ to the radius predicted by (22).

In order to compare our level set computations to (22), we must first decide which value to use for the "net interfacial tension" σ_n. According to (20), the net interfacial tension σ_n is represented as

$$\sigma_n = \frac{(\rho_w - \rho_o) g V^2}{2\pi^2 R_f^4}. \tag{66}$$

As exemplified by (41), (66) is only valid for large volumes of oil. In Table IV, we show computed values of the "effective" net interfacial tension $\sigma_n(V)$ for progressively larger volumes of oil. Our computed values of $\sigma_n(V)$ are derived by first finding R_f using our "energy minimization approach" and then substituting R_f back into (66). As predicted by (41), our computed values of $\sigma_n(V)$ approach the ideal value

$$\sigma_n(\infty) = \gamma(1 + \sin(\theta - \pi/2)), \tag{67}$$

in the limit as volume gets very large.

Given either the "effective" net interfacial tension $\sigma_n(V)$ (66), or the ideal value $\sigma_n(\infty)$ (67), we are in a position to determine the spreading constant k_1, defined by (22). In Tables V and VI, we display our computed values for k_1 when all the parameters V, Q, μ_o, γ and θ are varied. We used the "effective" net interfacial tension $\sigma_n(V)$ (66) in determining the values for k_1 in Table V and we used the ideal value $\sigma_n(\infty)$ (67) when determining the values for k_1 in Table VI. According to Izumiyama et al. [9], k_1 can be expressed as

$$k_1 = \left(\frac{k_0}{\pi^3}\right)^{1/8}, \tag{68}$$

with $k_0 = 1/2$. In Tables V and VI, we see that k_1 differs from the theoretical value of $k_1 = 0.60$ by a maximum of 5%.

VII. DISCUSSION OF RESULTS

As illustrated by Tables IV, V and VI, the spreading rate k and final oil slick radius R_f depend on the oil-water interfacial tension γ and the contact angle θ. The theoretical model for the spreading rate of oil under ice (22) is derived under the assumption that the net interfacial tension is related to the final spreading radius R_f by (66); this is valid for relatively large volume spills as

explained by (41). In Table IV, it is shown that the "effective" net interfacial tension $\sigma_n(V)$ as derived from R_f approaches the ideal value $\sigma_n(\infty)$ for large values of V. In Table VI, we see that the spreading constant k_1 is very close to the predicted value $k_1 = 0.60$ for $V \geq 1500\text{cm}^3$.

In order for practitioners to predict the extent of oil spreading, it is important to not only know the viscosity, density, and volume of oil, but also to know γ and θ. To this end, Liukkonen [11] has done extensive experiments on oil droplets submerged under ice in order to determine the relative surface energies of the oil, ice and water. Although, Liukkonen's work was thorough, there are still some unanswered questions as to the effect of interfacial tension and wall adhesion on the spreading rate.

One question is related to the possibility that there is a thin layer of water separating the oil from the ice. If there is a thin layer of water between the oil and ice, i.e. $\theta = 180^0$, how much effect does this have on the spreading rate k and final spreading radius R_f of a body of oil spreading under ice? In Figure 13, we compare the computed steady profile of a 0.2cm^3 oil droplet under ice for contact angles of 160^0, 170^0, and 180^0. The fact that these results are close to each other lends to the plausibility that one can measure a contact angle that is less than 180^0 by accident. We increased the resolution for the 180^0 case up to $N = 3500$! In figure 14, we display a blow-up of the free surface profile for computations of $N = 256$ and $N = 3500$ near $z = 0$. The two computations are in good agreement until $z < 0.0006\text{cm}$. In other words, if there was a layer of water separating the oil from the ice, it would be indistinguishable to the naked eye; in fact the water layer would probably be less than six microns thick. We remark that while on the one hand, the shape of static oil droplets in Liukkonen's experiments are insensitive to large contact angles, the spreading rate k and final slick radius R_f are also insensitive to large contact angles. In Table VI, we report that the spreading constant k varies by less than 2% when the contact angle ranges from 160^0 to 175^0. In Figure 15 we plot the spreading constant k versus θ where k is derived from the theoretical model (22). In order to derive k from (22), we used the "ideal" value for σ_n (67). In Figure 16, we plot the final spreading radius R_f versus θ where R_f is derived using the "Energy minimization approach" with $V = 3000\text{cm}^3$.

Another question is related to the fact that although we have a representative value for γ from Liukkonen's work, $\gamma = 49.2\text{g/s}^2$, this does not necessarily represent the values associated with the oil used in the experiments by either Yapa et al. or Izumiyama et al. According to Uzuner et al. [19], γ may take on values ranging from 15.8g/s^2 to 69g/s^2. The spreading rate k and the final spreading radius R_f both depend on γ. In Figure 17, we plot our computed spreading rate k versus γ for $\theta = 160^0$. We also plot in Figure 17 the spreading rate k predicted by (22) versus γ. In Figure 18, we plot the final spreading radius R_f versus γ where R_f is derived using the "Energy minimization approach" with $V = 3000\text{cm}^3$ and $160^0 \leq \theta \leq 180^0$.

As a final remark, it is possible for one to predict the overall net interfacial tension $\sigma_n(\infty)$ of an oil by measuring experimental values for R_f for different volumes of oil. If one pours a large enough volume of oil under ice, then one can find $\sigma_n(\infty)$ directly from a single experimental value of R_f using (20). Unfortunately, as shown in Table IV, one would need an "ice tank" that is at least 6 meters in diameter[2] in order for (20) to accurately predict $\sigma_n(\infty)$ to within two significant digits. For multiple measurements of R_f using smaller volumes of oil, one can fit the measured values of R_f to curves relating R_f to γ. As an example for measuring $\sigma_n(\infty)$ from experimental results, we consider the experimental results reported in Table 1 of Izumiyama et al. [9] The average value[3] for R_f from their experiments is 26.9cm for $V = 3000\text{cm}^3$ and 37.3cm for $V = 6000\text{cm}^3$. In Figure 18, we plot R_f versus γ for $V = 3000\text{cm}^3$ and $160^0 \leq \theta \leq 180^0$. In Figure 19, we plot R_f versus γ for $V = 6000\text{cm}^3$ and $160^0 \leq \theta \leq 180^0$. Our resulting best fit using the data found in the experiments of Izumiyama et al. was,

$$\sigma_n(\infty) = 117 \tag{69}$$

$$\gamma = 59\text{g/s}^2 \tag{70}$$

$$\theta = 170^0. \tag{71}$$

VIII. CONCLUSION

We have presented an adaptive level set numerical method for computing the spreading rate of oil under ice. We have also presented a very accurate and efficient "energy minimization approach" for determining the final spreading radius and free-surface profile of a body of oil under ice. Our methods agree well with experiments and theory. Differences between our methods and experiments are due to lack of information regarding the oil-water interfacial tension γ and also the contact angle θ. In section VII, we examine the sensitivity of the spreading rate k and the final spreading radius R_f when the oil/water interfacial tension γ or the contact angle θ are varied. In future work, it is necessary to do more realistic simulations of oil spills. For example, surface roughness and temperature were not taken into account in our numerical models. Also, the scenario of a moving ice cover and non-axisymmetric ice configuration will necessitate fully 3d simulations.

---

[2]The ice model basin at the Ship Research Institute has dimensions of 35m by 6m in length and width respectively

[3]We did not include the result from test 3 when computing the average, since this result was not consistent with the other results; probably due to asymmetry in the results

IX. ACKNOWLEDGEMENTS

Work supported in part by an STA Fellowship, NSF # DMS 97-06847, the Ship Research Institute, Tokyo, Japan, and the Dept. of Math, UCD, Davis, CA 95616.

---

[1] A. S. Almgren, J. B. Bell, P. Colella, L. H. Howell, and M. Welcome. A high-resolution adaptive projection method for regional atmospheric modeling. In *Proceedings of the U.S. EPA NGEMCOM Conference*, August 1995.

[2] A. S. Almgren, J. B. Bell, and W. G. Szymczak. A numerical method for the incompressible Navier-Stokes equations based on an approximate projection. *SIAM J. Sci. Comput.*, 17(2), March 1996.

[3] J. B. Bell, M. J. Berger, J. S. Saltzman, and M. L. Welcome. Three-dimensional adaptive mesh refinement for hyperbolic conservation laws. *SIAM J. Sci. Comput.*, 15(1):1277–138, January 1994.

[4] J. B. Bell, P. Colella, and H. M. Glaz. A second-order projection method for the incompressible Navier-Stokes equations. *J. Comput. Phys.*, 85:257–283, December 1989.

[5] J. B. Bell and D. L. Marcus. A second-order projection method for variable-density flows. *J. Comput. Phys.*, 101:334–348, 1992.

[6] M. J. Berger and I. Rigoustsos. An algorithm for point clustering and grid generation. Technical Report NYU-501, New York University-CIMS, 1991.

[7] J. U. Brackbill, D. B. Kothe, and C. Zemach. A continuum method for modeling surface tension. *J. Comput. Phys.*, 100:335–353, 1992.

[8] Y.C. Chang, T.Y. Hou, B. Merriman, and S. Osher. Eulerian capturing methods based on a level set formulation for incompressible fluid interfaces. *J. Comput. Phys.*, 124:449–464, 1996.

[9] K. Izumiyama, S. Uto, S. Narita, and R. Tasaki. Effects of interfacial tension on the spreading of oil under an ice cover. In *Proceedings of the 14th International Symposium on Ice, IAHR 98*, July 1998. Clarkson, University.

[10] E.Y. Kniazeva. Calculation of oil spreading in water surroundings under ice. Master's thesis, Saint Petersburg State Technical University, 1996.

[11] S. Liukkonen. Adhesion between oil and ice. Technical Report VALB160, VTT Manufacturing Technology, 1996.

[12] S. Osher and J. A. Sethian. Fronts propagating with curvature-dependent speed: Algorithms based on hamilton-jacobi formulations. *J. Comput. Phys.*, 79(1):12–49, 1988.

[13] M. Sussman, A. Almgren, J. Bell, P. Colella, L. Howell, and M. Welcome. An adaptive level set approach for incompressible two-phase flows. *J. Comput. Phys.* accepted for publication, 1998.

[14] M. Sussman, E. Fatemi, P. Smereka, and S.J. Osher. An improved level set method for incompressible two-phase flows. *Journal of Computers and Fluids*, 27(5-6):663–680, 1998.

[15] M. Sussman and P. Smereka. Axisymmetric free boundary problems. *J. Fluid Mech.*, 341:269–294, 1997.

[16] M. Sussman, P. Smereka, and S.J. Osher. A level set approach for computing solutions to incompressible two-phase flow. *J. Comput. Phys.*, 114:146–159, 1994.

[17] O. Tatebe. The multigrid preconditioned conjugate gradient method. In *6th Copper Mountain Conference on Multigrid Methods*, Copper Mountain, CO, April 4–9 1993.

[18] S. O. Unverdi and G. Tryggvason. A front-tracking method for viscous, incompressible, multi-fluid flows. *J. Comput. Phys.*, 100:25–37, 1992.

[19] M.S. Uzuner, F.B. Weiskopf, J.C. Cox, and L.A. Schultz. Transport of oil under smooth ice. Technical Report EPA-600/3-79-041, ARCTEC Incorporated, Columbia, Maryland, USA, 1979.

[20] P.D. Yapa and T. Chowdhury. Oil spreading under ice covers. In *Proceedings of the 1989 Oil Spill Conference*, pages 161–166, 1989.

[21] H. Zhao, B. Merriman, S. Osher, and L. Wang. Capturing the behavior of bubbles and drops using the variational level set approach. Technical Report CAM Report 96-39, University of California, Los Angeles, 1996. submitted to JCP.

TABLE I. Convergence study using the Level Set Method, oil droplet relaxation, $\gamma = 49.2\text{g/s}^2$, $\theta = 160^o$; θ_i and r_i are the initial contact angle and contact position respectively, θ_f and r_f are the final contact angle and contact position respectively.

Δx	θ_i	r_i	r_f	θ_f
3/32	90	0.4567	0.2037	158.7
3/64	90	0.4567	0.2270	158.7
3/128	90	0.4567	0.2299	159.6
3/128	160	0.1244	0.2299	159.6

TABLE II. Convergence study using the "energy minimization approach," oil droplet relaxation, $\gamma = 49.2\text{g/s}^2$, $\theta = 160^o$; r_f and θ_f represent the final contact position and final contact angle respectively.

N	r_f	θ_f
64	0.2293	158.4
128	0.2288	159.4
256	0.2287	159.8

TABLE III. Comparison between computations and experiments; the spreading constant k is computed using the adaptive level set approach. The final slick radius R_f is computed using the "energy minimization approach." All data is given in cgs units. k^c and R_f^c represent the computed values for the spreading coefficient k and final slick radius R_f respectively. k^e and R_f^e represent the experimental values for k and R_f respectively.

V	Q	μ_o	γ	θ	k^c	R_f^c	k^e	R_f^e
3000	24.6	2.54	49.2	160	0.46	27.8	0.45	26.7
3000	12.3	2.54	49.2	160	0.42	27.8	0.41	28.1
778	8.1	6.05	49.2	160	0.43	14.4	N/A	N/A
880	58.7	1.79	49.2	160	0.50	15.5	N/A	N/A

TABLE IV. Relation between the "effective" net interfacial tension $\sigma_n(V)$ and V. $\sigma_n(\infty) = \gamma(1+\sin(\theta-\pi/2))$ represents the ideal net interfacial tension in the limit as V becomes infinite. $\gamma = 49.2$, $\rho_w - \rho_o = 0.123$. All data is given in cgs units.

V	θ	R_f	$\sigma_n(V)$	$\sigma_n(\infty)$
1000	160	16.1	90.1	95.4
3000	160	27.8	92.3	95.4
30000	160	87.3	94.4	95.4
300000	160	275.7	95.1	95.4
1000	180	16.0	92.8	98.4
3000	180	27.6	95.1	98.4
30000	180	86.7	97.3	98.4
300000	180	273.6	98.1	98.4

TABLE V. Computational results for the spreading constant k_1; the predicted value for k_1 is 0.60. $\sigma_n(V)$ is used in determining k_1. All data is given in cgs units.

V	Q	μ_o	γ	θ	$\sigma_n(V)$	k	k_1
3000	24.6	2.54	49.2	175	94.9	0.45	0.60
3000	24.6	5.08	49.2	175	94.9	0.48	0.60
3000	12.3	2.54	49.2	175	94.9	0.41	0.58
1500	24.6	2.54	49.2	175	93.6	0.44	0.58
3000	24.6	2.54	49.2	160	92.3	0.46	0.61
3000	12.3	2.54	49.2	160	92.3	0.42	0.59
1500	24.6	2.54	49.2	160	91.0	0.45	0.59
1500	24.6	2.54	16.0	160	30.4	0.56	0.62
1500	24.6	2.54	32.0	160	60.0	0.50	0.61
1500	24.6	2.54	64.0	160	117.2	0.43	0.59
778	8.1	6.05	49.2	160	89.6	0.43	0.57
880	58.7	1.79	49.2	160	90.1	0.50	0.62

TABLE VI. Computational results for the spreading constant k_1; the predicted value for k_1 is 0.60. $\sigma_n(\infty)$ is used in determining k_1. All data is given in cgs units.

V	Q	μ_o	γ	θ	$\sigma_n(\infty)$	k	k_1
3000	24.6	2.54	49.2	175	98.2	0.45	0.60
3000	24.6	5.08	49.2	175	98.2	0.48	0.60
3000	12.3	2.54	49.2	175	98.2	0.41	0.59
1500	24.6	2.54	49.2	175	98.2	0.44	0.59
3000	24.6	2.54	49.2	160	95.4	0.46	0.61
3000	12.3	2.54	49.2	160	95.4	0.42	0.60
1500	24.6	2.54	49.2	160	95.4	0.45	0.60
1500	24.6	2.54	16.0	160	31.0	0.56	0.62
1500	24.6	2.54	32.0	160	62.1	0.50	0.61
1500	24.6	2.54	64.0	160	124.1	0.43	0.60
778	8.1	6.05	49.2	160	95.4	0.43	0.58
880	58.7	1.79	49.2	160	95.4	0.50	0.63

List of Figures

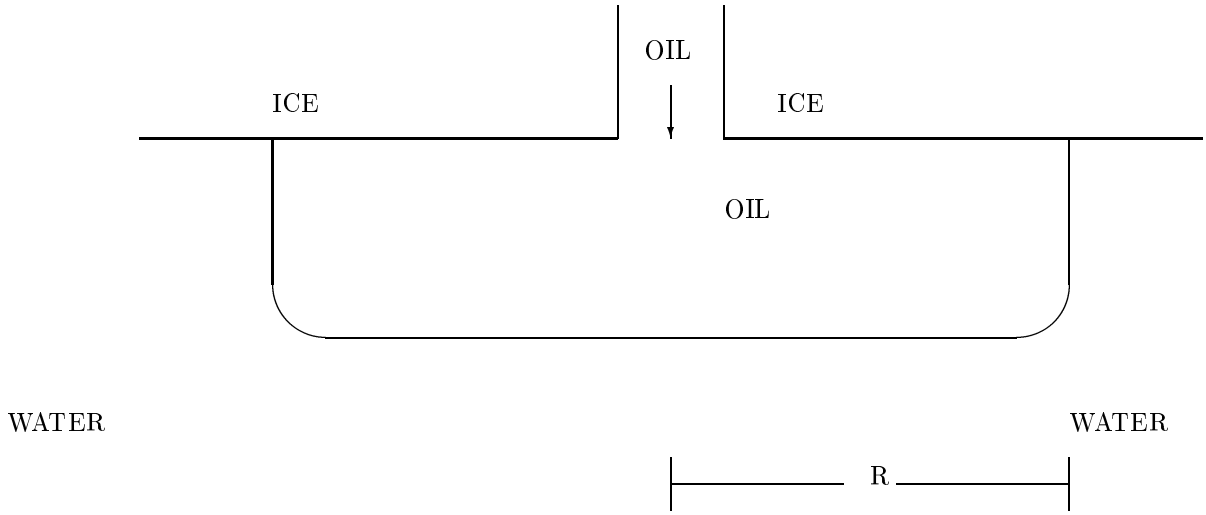

FIG. 1. Diagram of axi-symmetrical spreading of oil underneath a solid ice cover.

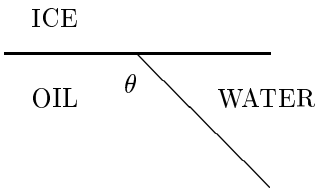

FIG. 2. Diagram of oil/water interface meeting at the ice. The contact angle θ is typically 160^0 for oil in water underneath ice.

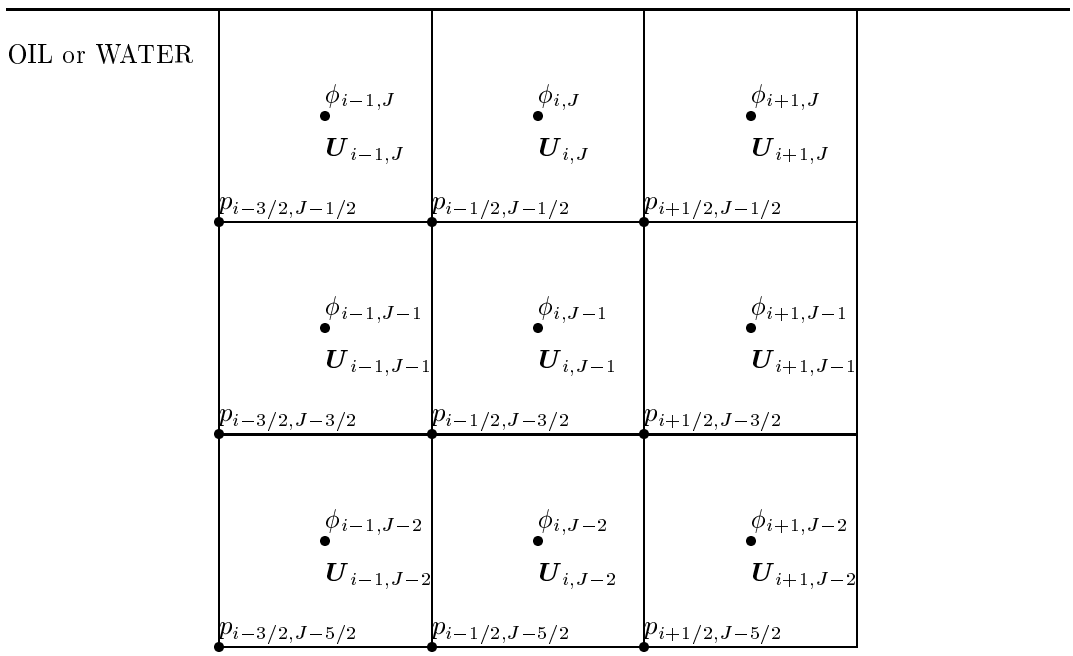

FIG. 3. Diagram of where the discrete variables $\boldsymbol{U}$, p and ϕ are located in relation to the computational grid and the physical boundary.

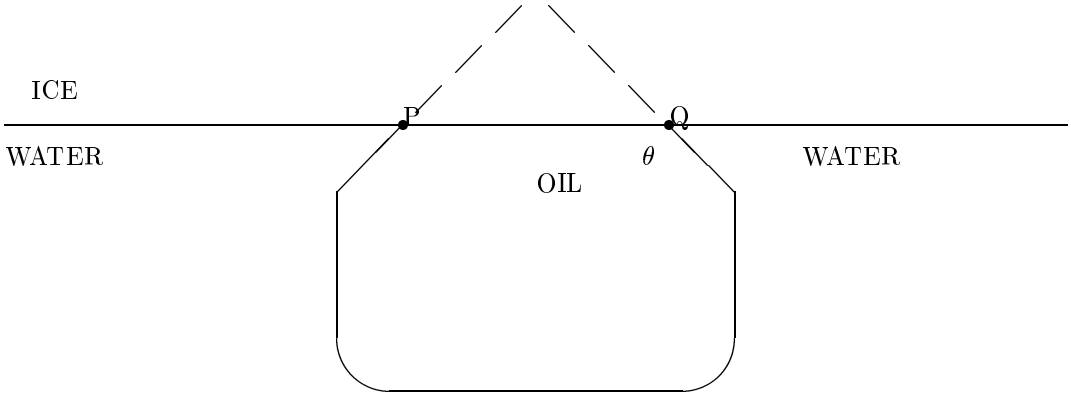

FIG. 4. Diagram of oil/water interface meeting at the ice. The dashed line represents the imaginary interface used for redistancing purposes.

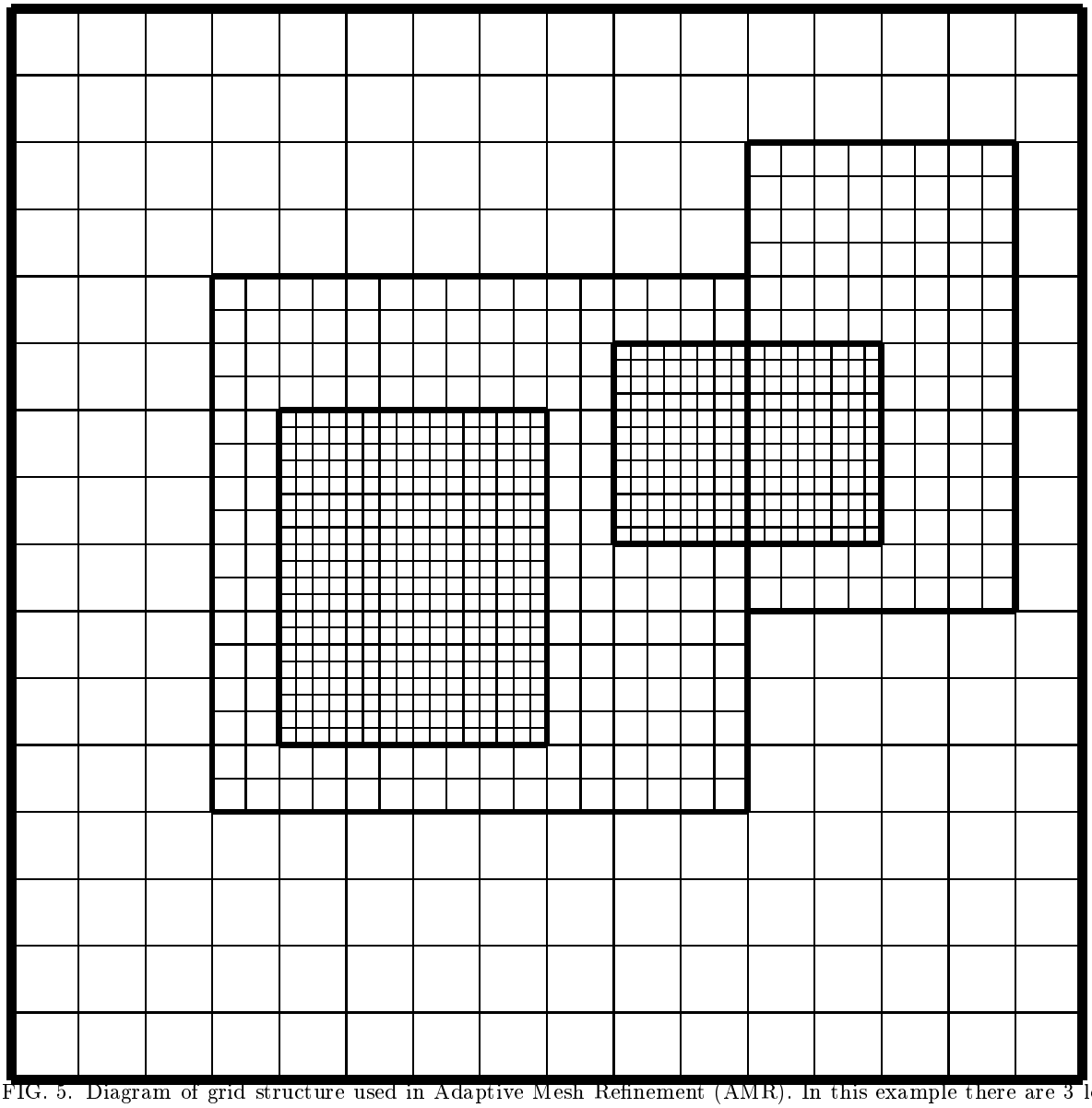

FIG. 5. Diagram of grid structure used in Adaptive Mesh Refinement (AMR). In this example there are 3 levels. Level 0 has one 16x16 grid. Level 1 has two grids; a 16x16 grid and a 8x14 grid. Level 2 also has two grids; a 16x20 grid and a 16x12 grid. The refinement ratio between levels in this example is 2.

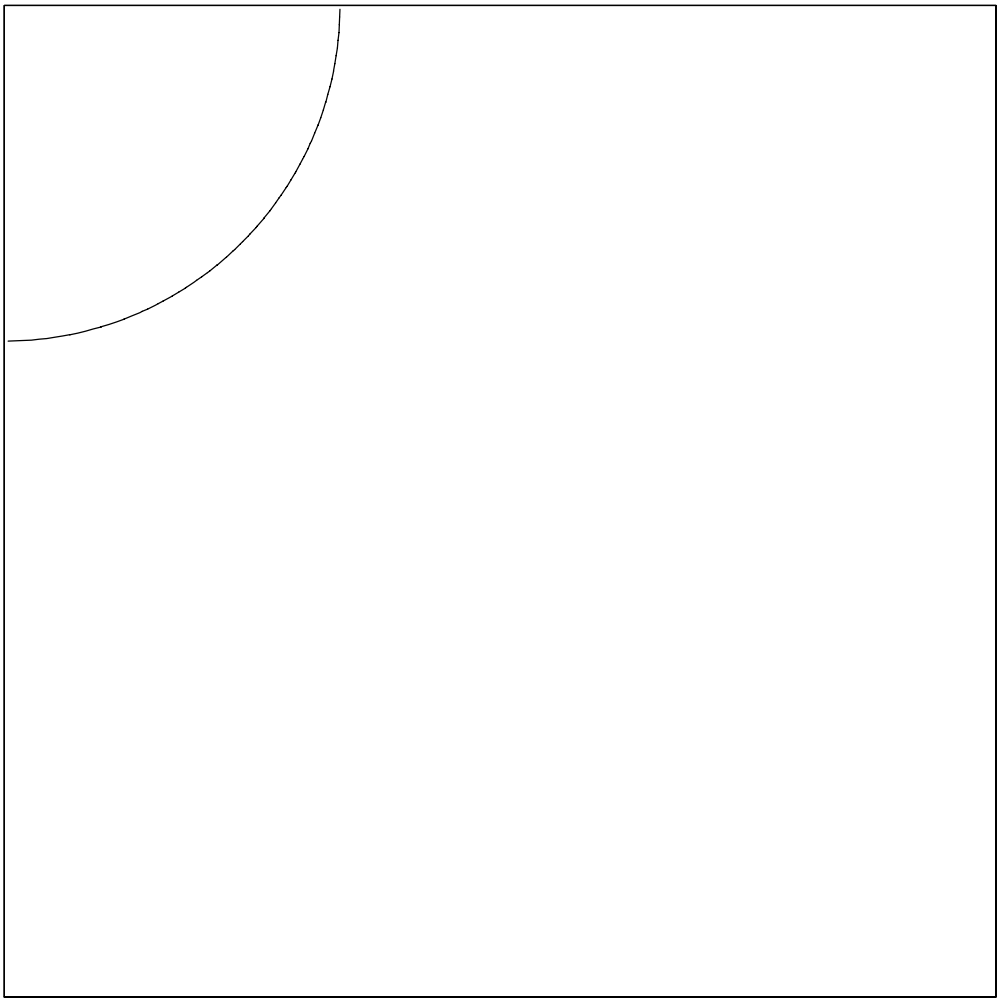

FIG. 6. Initial interface for oil droplet underneath layer of ice in water. Initial angle is 90^0. grid resolution is 128x128.

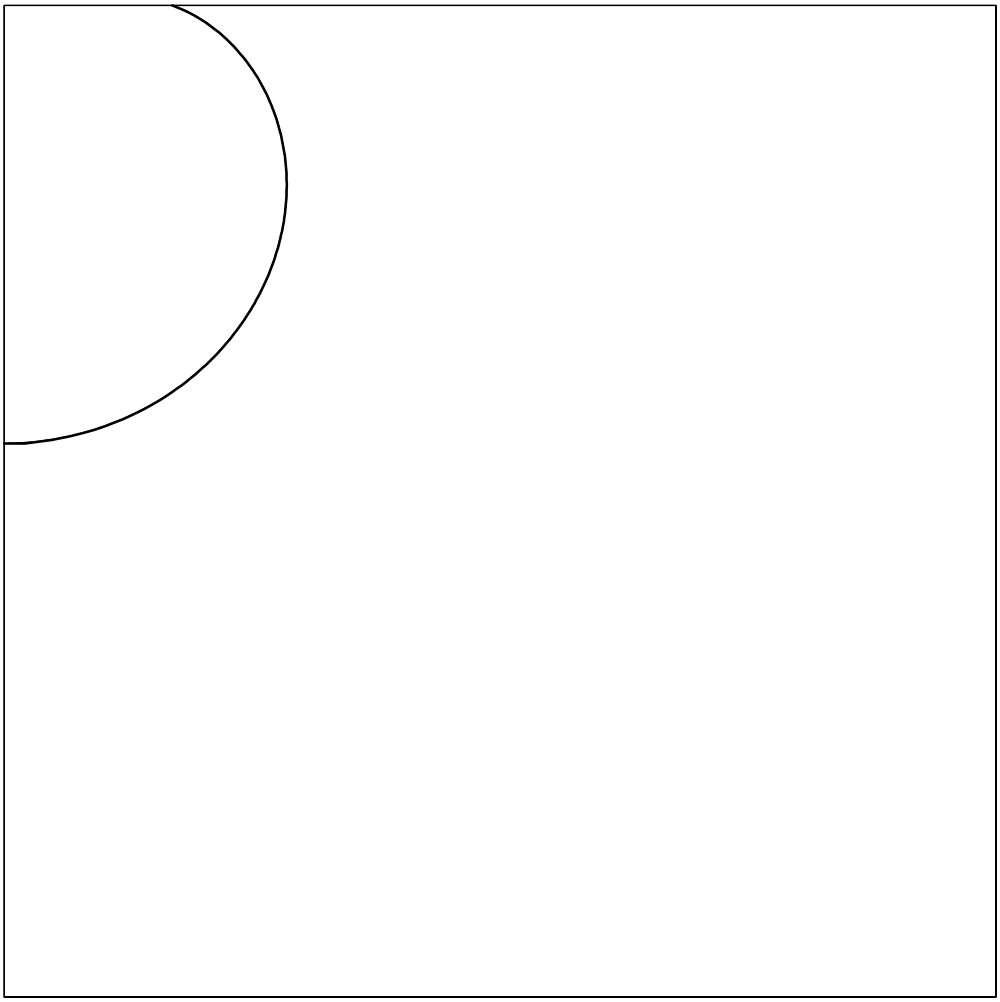

FIG. 7. Steady state profile of interface for oil droplet underneath layer of ice in water. Initial angle was 90^0. grid resolution is 128x128. Results computed using the level set method (thin contour) are compared to results using the "energy minimization approach" (thick contour).

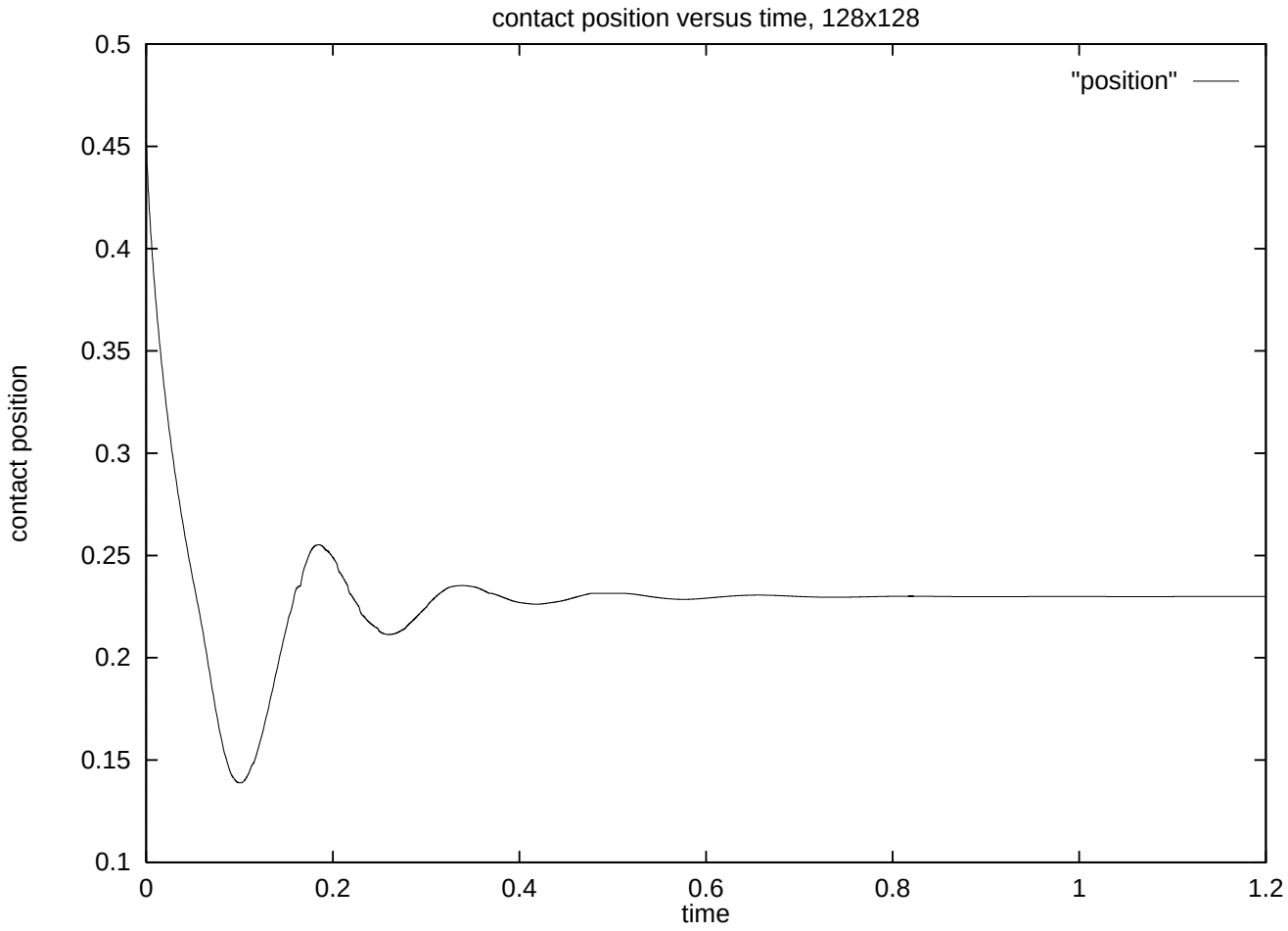

FIG. 8. Contact position versus time; 128x128 grid resolution. Initial angle is 90^0.

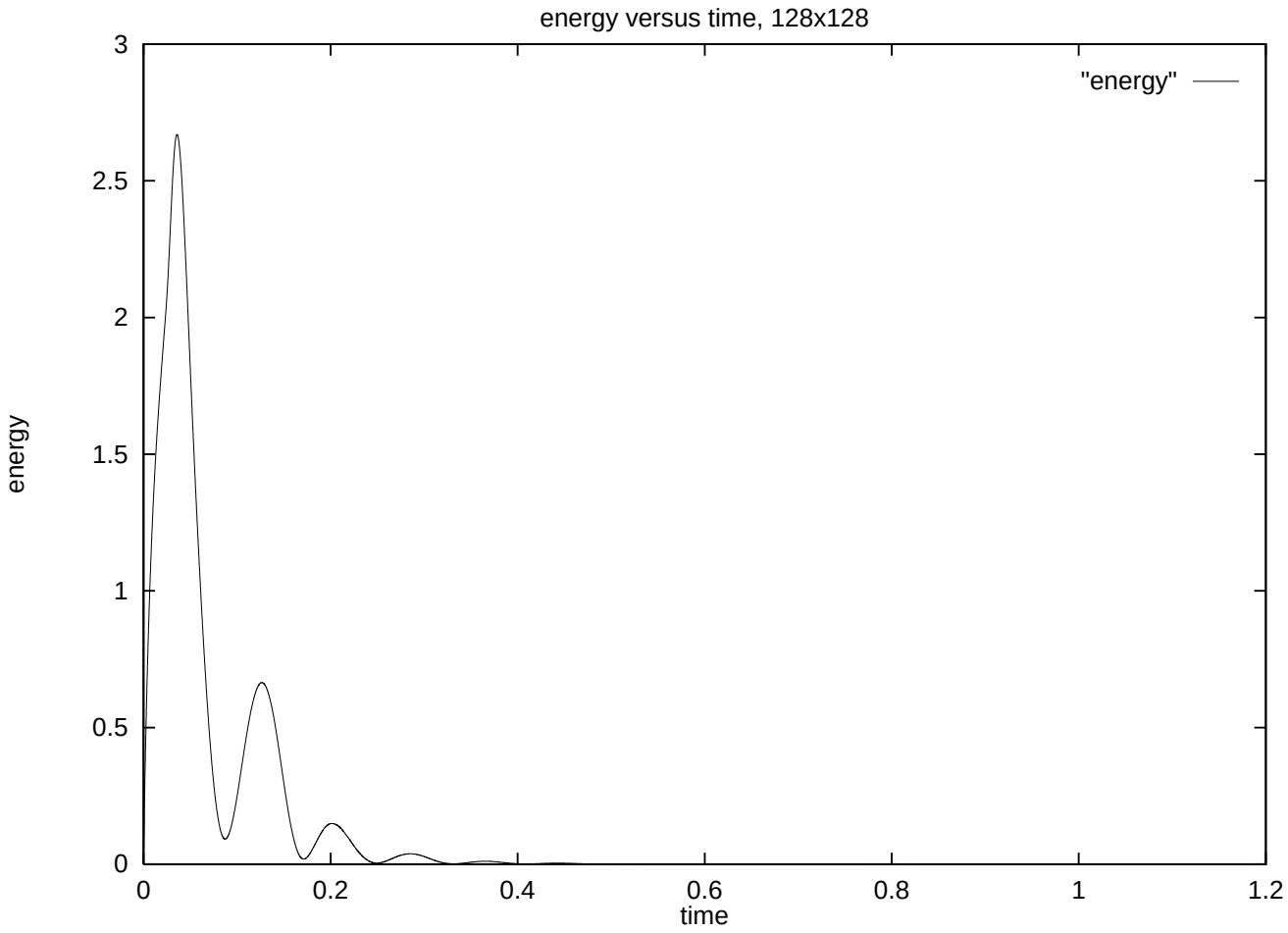

FIG. 9. kinetic energy versus time; 128x128 grid resolution. Initial angle is 90^0.

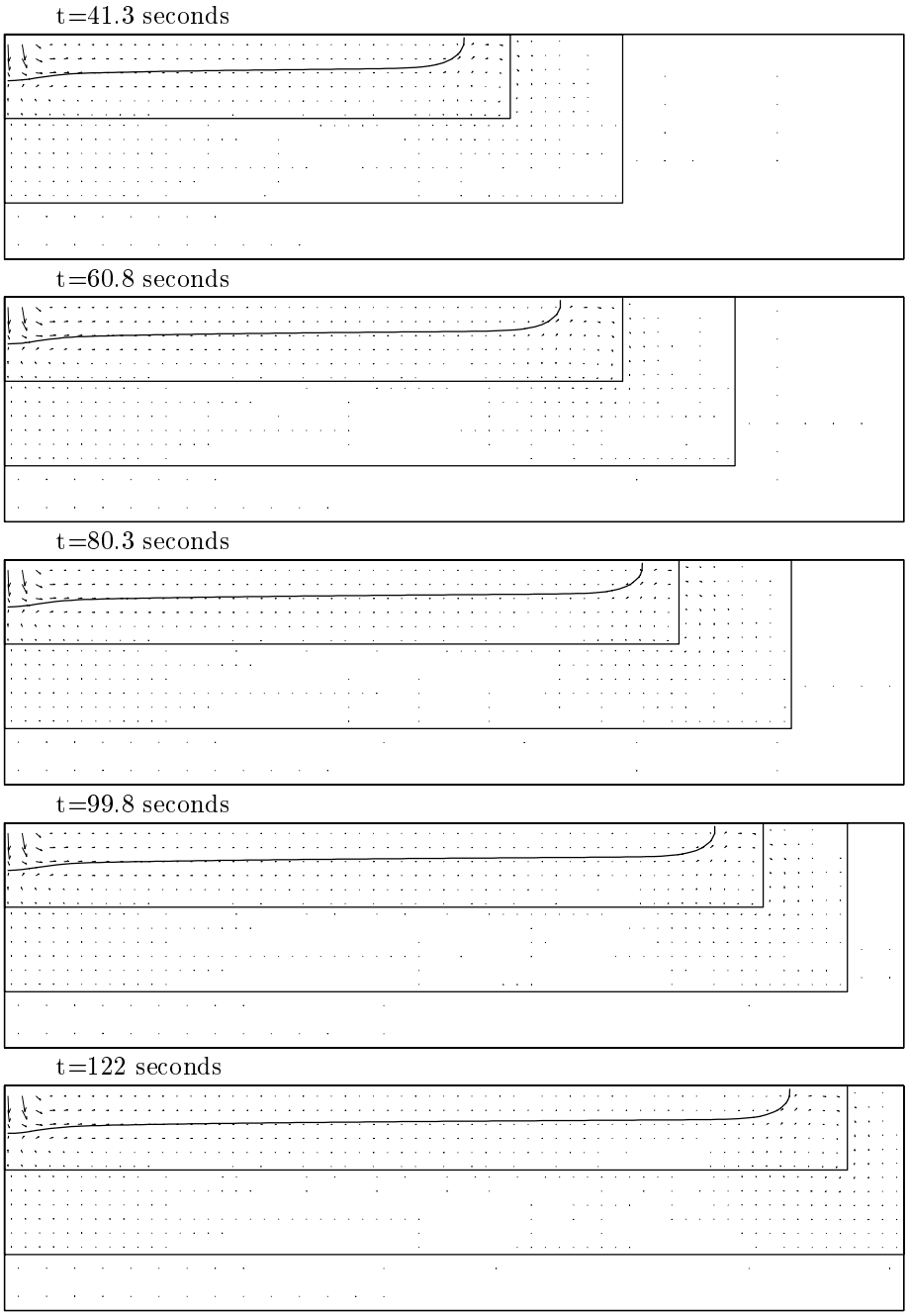

FIG. 10. The spreading of oil in water underneath ice. $\theta = 160^0$, $Q = 24.6\text{cm}^3/\text{s}$. Effective fine grid resolution is 128x32.

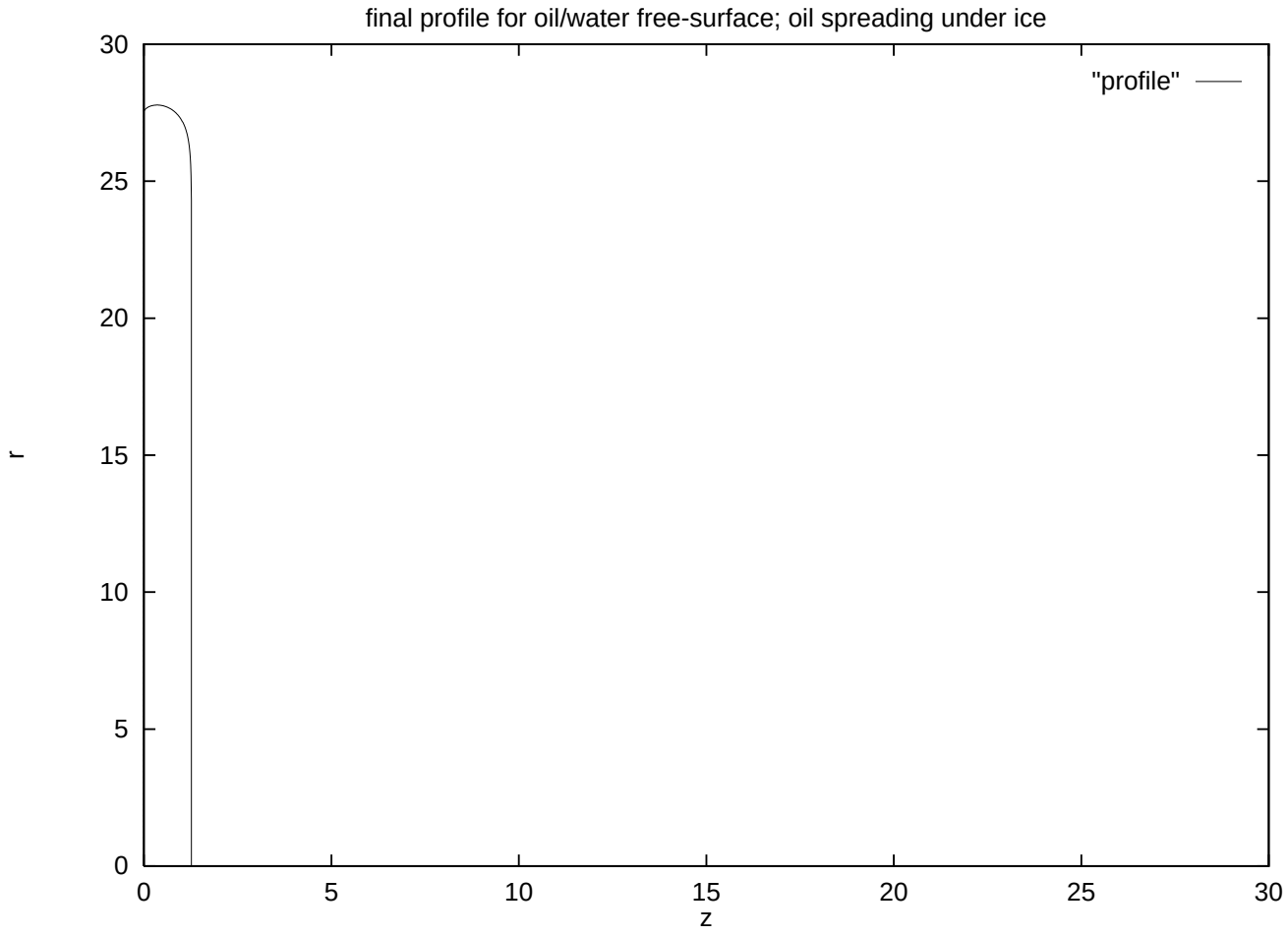

FIG. 11. Final profile of the oil/water free surface for oil spreading under ice; $V = 3000\text{cm}^3$, $\gamma = 49.2\text{g/s}^2$, $\theta = 160^o$. Computation performed using the "energy minimization approach" with $N = 128$. $z = 0$ represents the ice boundary.

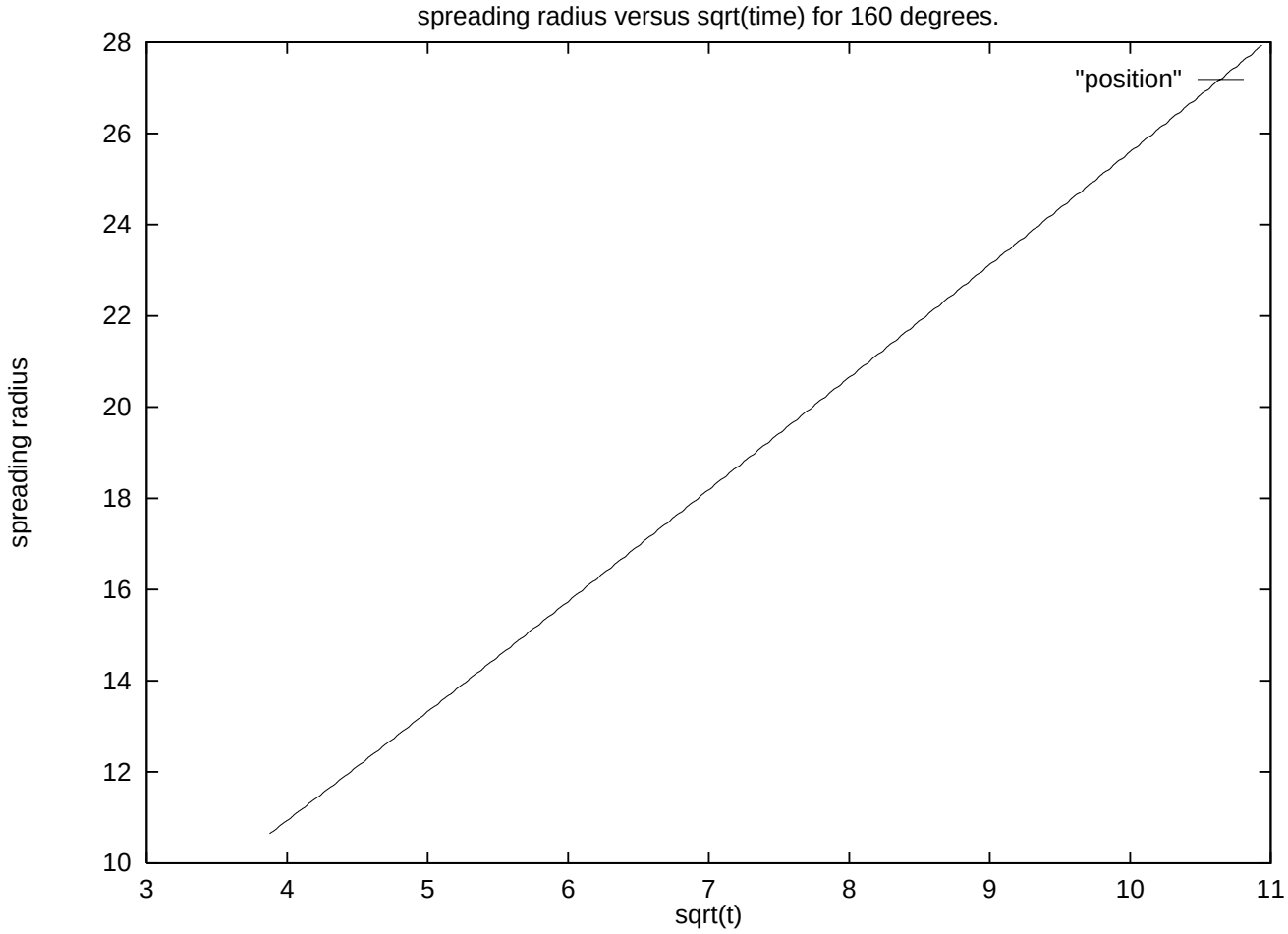

FIG. 12. graph of R versus $t^{1/2}$ for $\gamma = 49.2\mathrm{g/s}^2$ and $\theta = 160^o$.

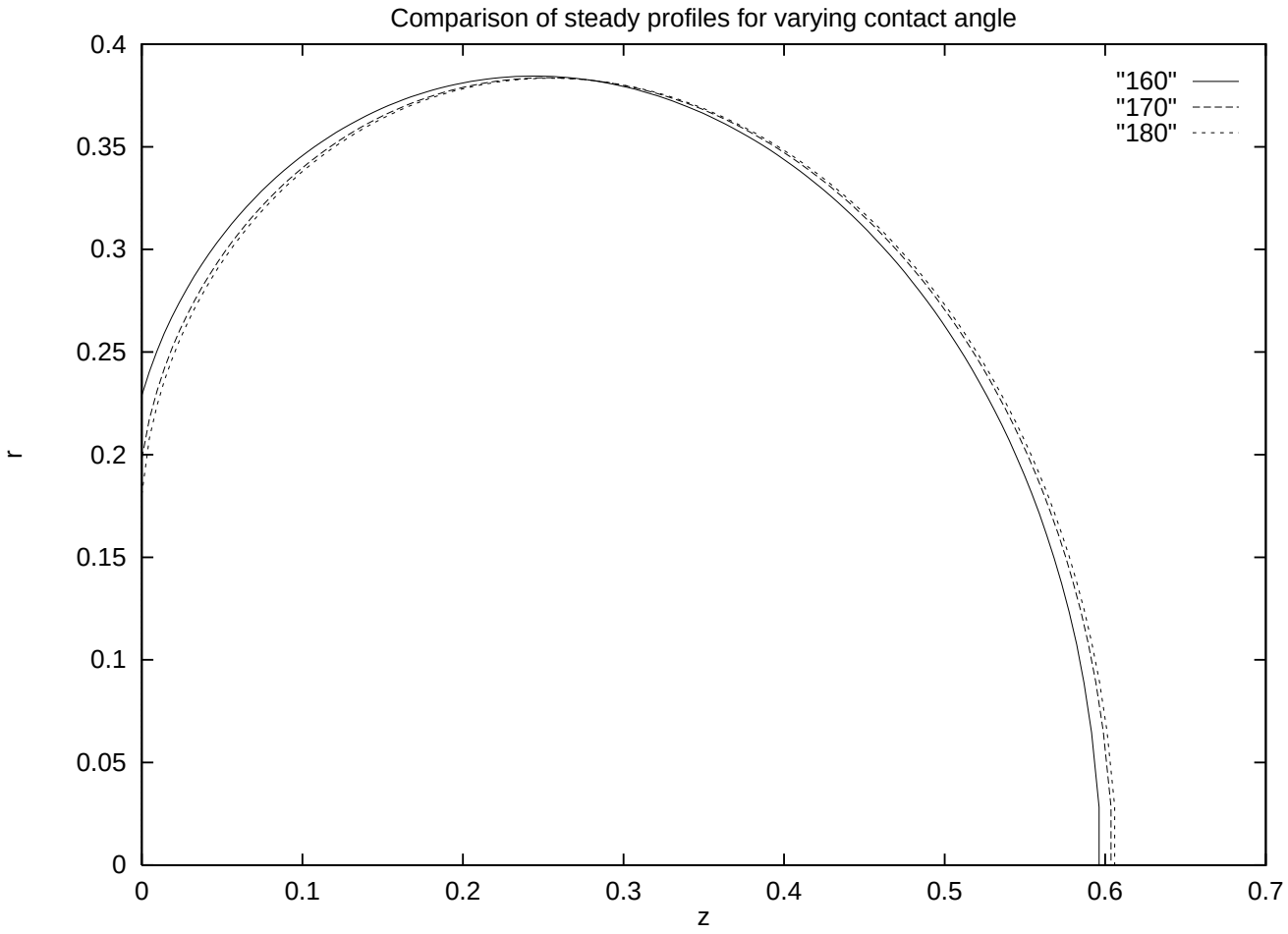

FIG. 13. Comparison of results for the final profile of 0.2cm^3 oil drop under ice. Results computed using the energy minimization approach with $N = 128$.

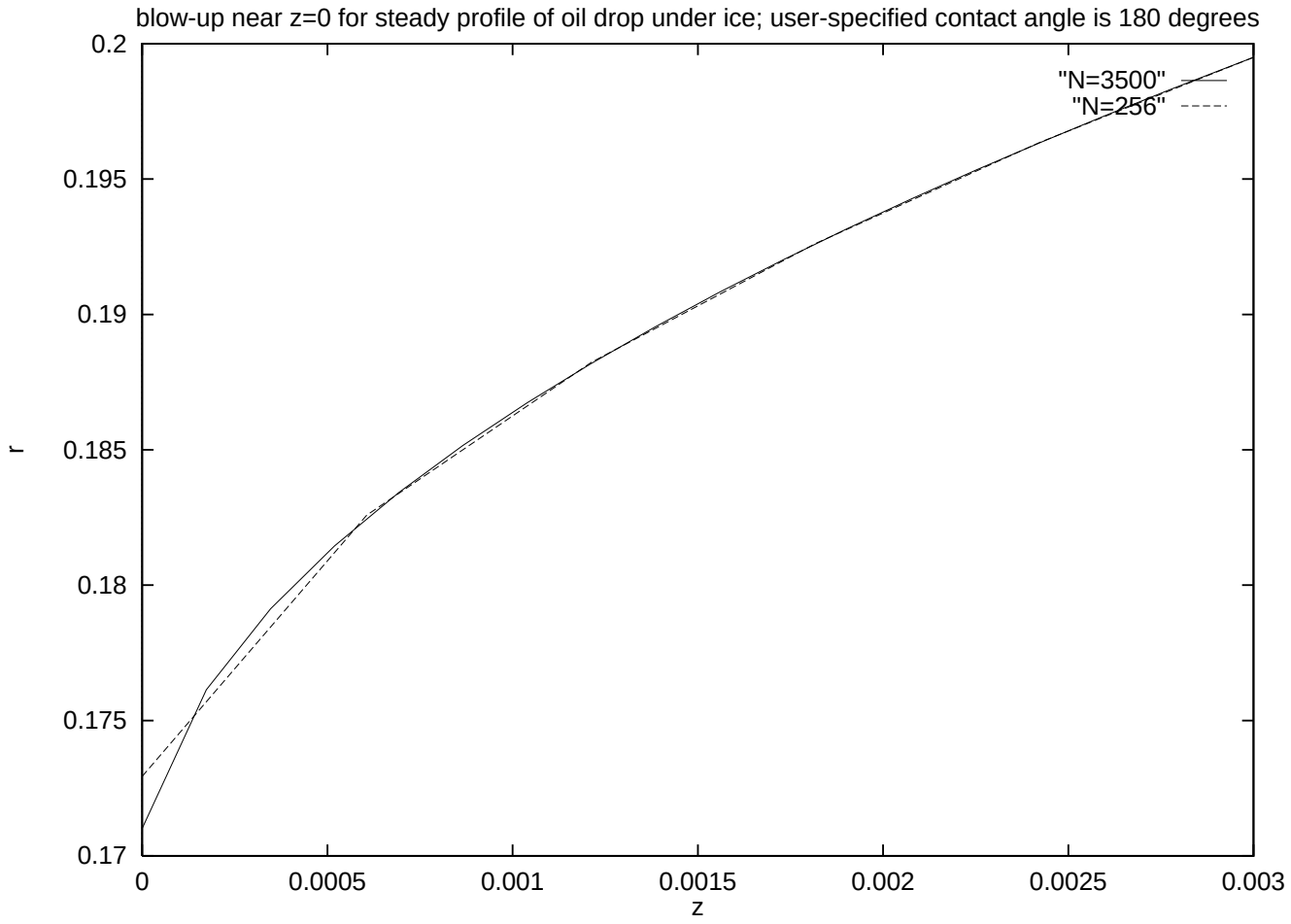

FIG. 14. Blow-up of oil/water profile near $z = 0$ for the final profile of a 0.2cm^3 oil drop under ice. The user-defined contact angle is 180^0. The results for $N = 256$ and $N = 3500$ agree well for values of z as small as 0.0006cm.

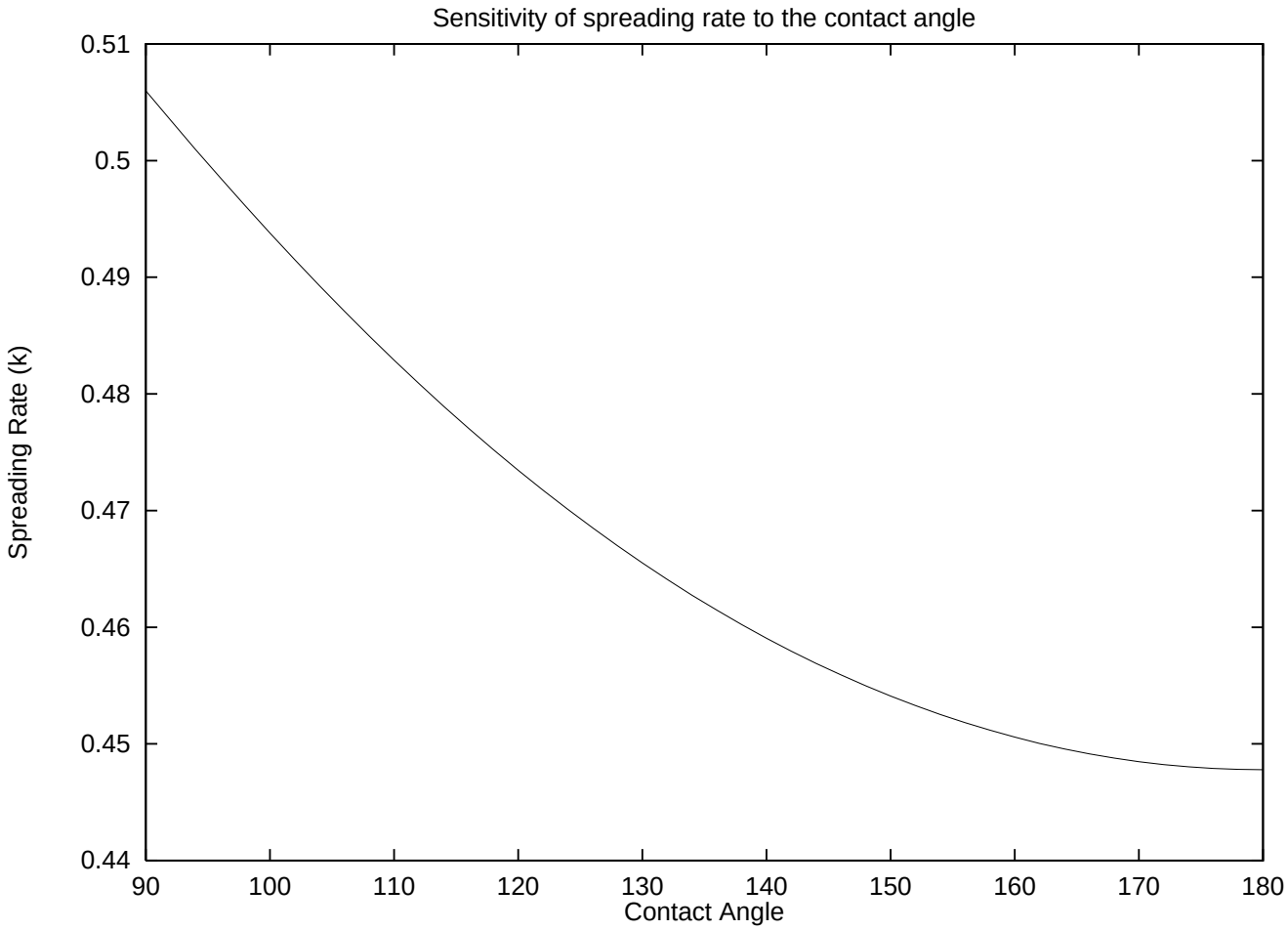

FIG. 15. Sensitivity of the spreading rate k to the contact angle θ ($\gamma = 49.2$).

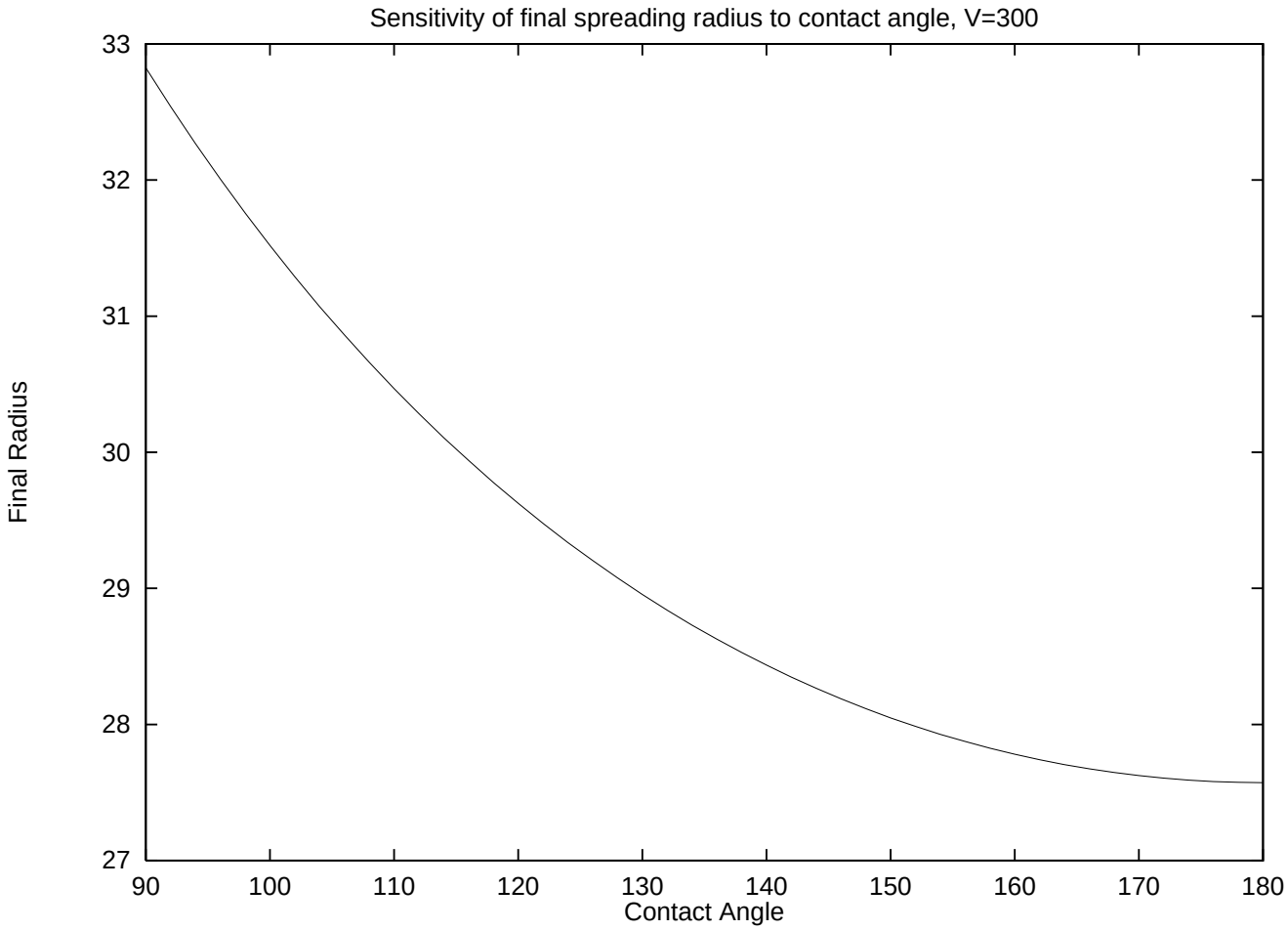

FIG. 16. Sensitivity of the Final Spreading Radius R_f to the contact angle θ; $V = 3000.0\text{cm}^3$, $\gamma = 49.2\text{g/s}^2$. R_f is computed using the "Energy Minimization Approach."

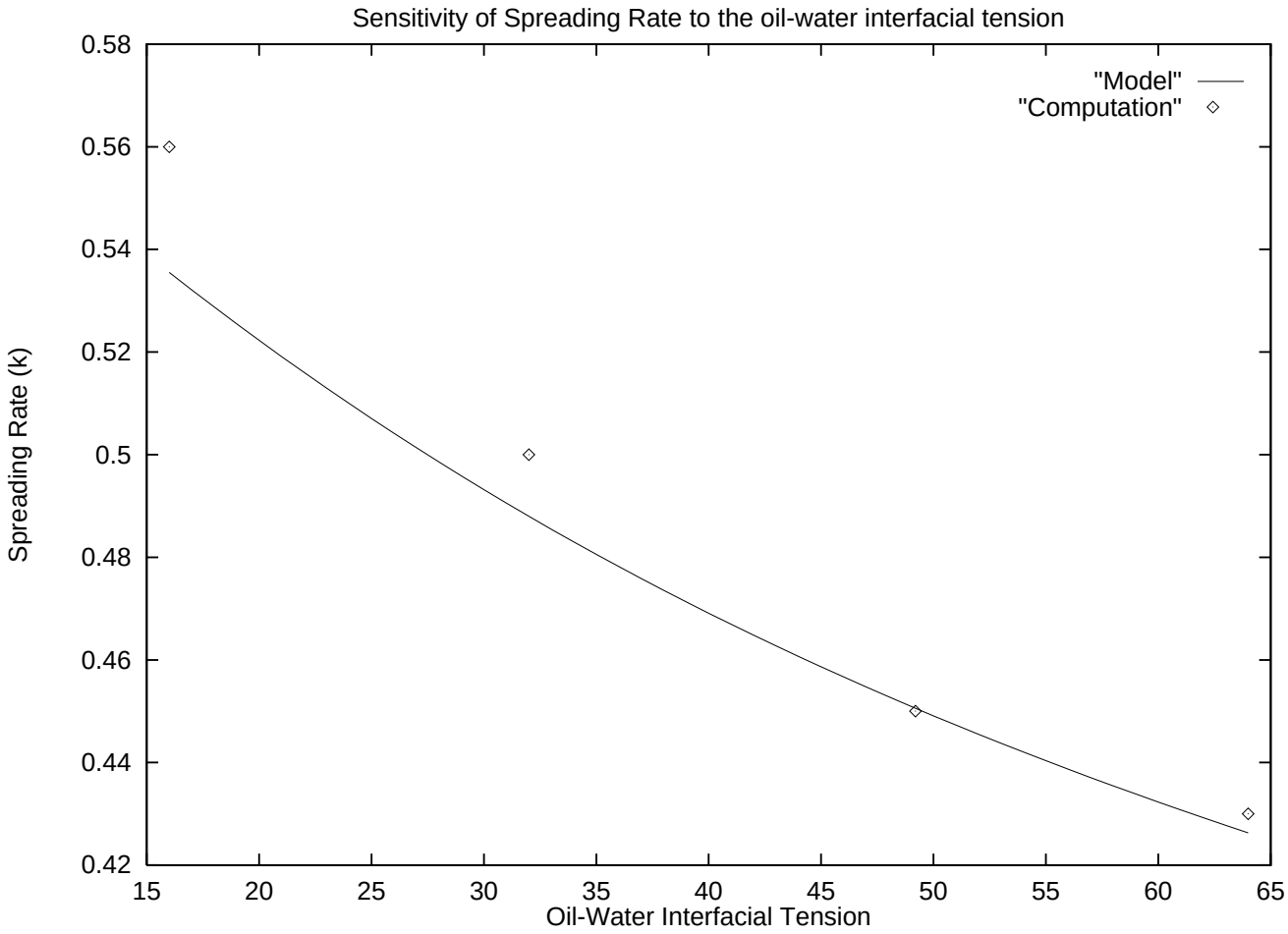

FIG. 17. Sensitivity of the spreading rate k to the Oil-water interfacial tension γ ($\theta = 160^0$). k is derived from the theoretical model of Izumiyama et al.

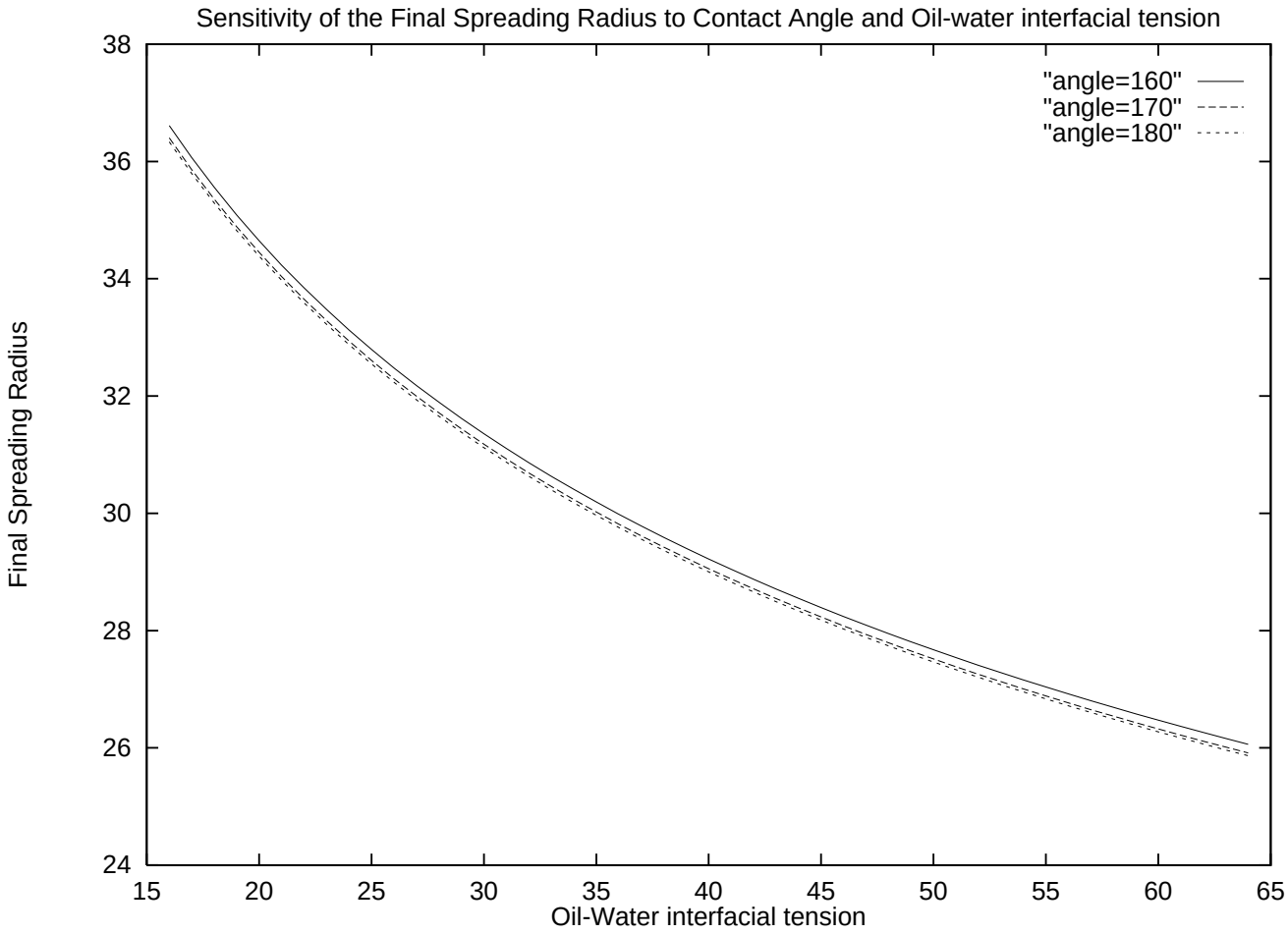

FIG. 18. Sensitivity of the Final Spreading Radius R_f to the Oil-water interfacial tension γ. $V = 3000.0\text{cm}^3$ and $160^0 \leq \theta \leq 180^0$. R_f is computed using the "Energy Minimization Approach."

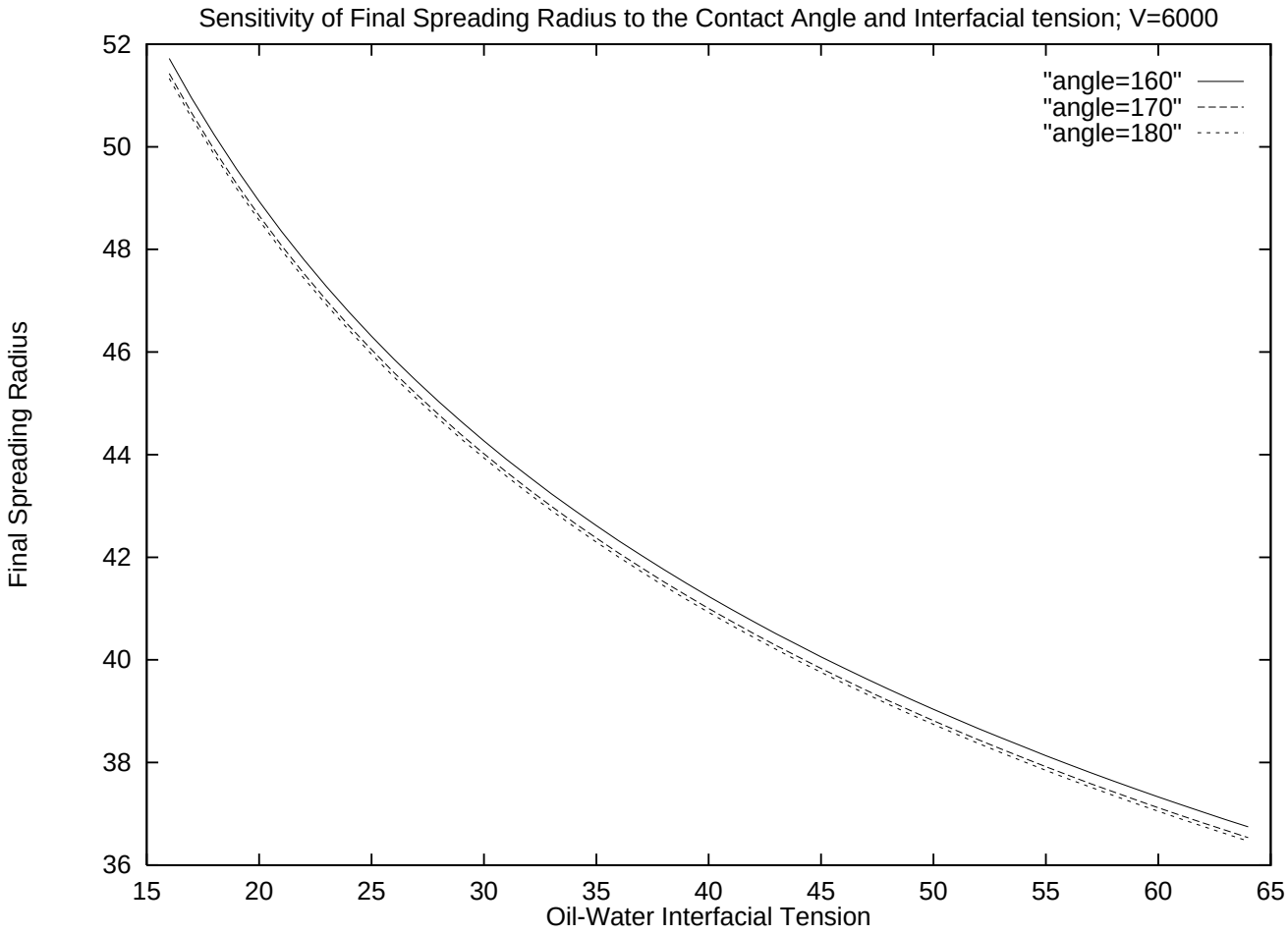

FIG. 19. Sensitivity of the Final Spreading Radius R_f to the Oil-water interfacial tension γ. $V = 6000.0\text{cm}^3$ and $160^0 \leq \theta \leq 180^0$. R_f is computed using the "Energy Minimization Approach."